

# A Semi-Analytical Solution for Temperature Distribution in Friction Stir Welding

Armin Rahmati Darvazi (✉ [ammrah@guilan.ac.ir](mailto:ammrah@guilan.ac.ir))

University of Guilan

---

## Research Article

**Keywords:** Semi-analytical thermal model, Friction stir welding, Asymmetric distribution of temperature, Heat sources and sinks

**Posted Date:** June 1st, 2021

**DOI:** <https://doi.org/10.21203/rs.3.rs-521499/v1>

**License:**  This work is licensed under a Creative Commons Attribution 4.0 International License.

[Read Full License](#)

---

***Title page:***

***Title:*** A semi-analytical solution for temperature distribution in friction stir welding

***Name:*** Armin Rahmati Darvazi \*

***\* Corresponding author, PhD, Assistant professor***

***Email:*** [Armrah@Guilan.ac.ir](mailto:Armrah@Guilan.ac.ir)

***ORCID:*** 0000-0002-1498-451X

***Address:*** Faculty of Technology and Engineering, East of Guilan, University of Guilan,  
Rudsar, Iran.

## A semi-analytical solution for temperature distribution in friction stir welding

### Abstract

In this paper, a semi-analytical thermal model of friction stir welding processes is developed in which the heat-generating regions are divided into many elements as point heat sources. The heat generation in each element involves the friction and plastic deformation, and the temperature rise caused by each element is calculated by solving the heat conduction equation of a moving heat source in a solid body. The heat loss through the top and bottom surfaces are considered in the model as heat sinks. The asymmetric distribution of the temperature is calculated through the whole process and over the whole volume of the workpiece by integrating the effects of all heat sources and sinks. The temperature-dependent material properties are updated by a numerical routine. The comparison between the calculated results and the experimental data clearly approved the validity of the proposed method for some aluminum and steel alloys.

*Keywords:* Semi-analytical thermal model; Friction stir welding; Asymmetric distribution of temperature; Heat sources and sinks

Nomenclature	
$C_p$	Specific heat capacity (J/kg°C)
$dQ$	Heat flux at each element (W/m <sup>2</sup> )
$H$	Plate thickness (m)
$h$	Coefficient of heat convection (W/ m <sup>2</sup> °C)
$k$	Thermal conductivity (W/m°C)
$K_n$	The modified Bessel function of the second kind and order $n$
$P$	The normal pressure of the tool (MPa)
$Q$	Heat flux (W/m <sup>2</sup> )
$R$	3D distance, $\sqrt{x^2 + y^2 + z^2}$ (m)

$r$	2D distance, $\sqrt{x^2 + y^2}$ (m)
$r_p$	Tool pin radius (m)
$r_s$	Tool shoulder radius (m)
$T$	Temperature ( $^{\circ}\text{C}$ )
$T_0$	Initial temperature ( $^{\circ}\text{C}$ )
$t$	Time (s)
$v$	Tool translational speed (m/s)
$(x, y, z)$ or $(w, y, z)$	Space coordinate(m)
$\alpha$	Thermal diffusivity ( $\text{m}^2/\text{s}$ )
$\delta$	Sticking state variable
$\eta$	Efficiency
$\Theta$	Angle (rad)
$\mu$	Friction coefficient
$\rho$	Density ( $\text{Kg}/\text{m}^3$ )
$\sigma_{yield}$	Yield tensile stress (MPa)
$\tau$	Yield shear stress (MPa)
$\Psi$	The advancing retreating factor
$\omega$	Tool rotational speed (rad/s)

## 1. Introduction

One of the solid-state joining processes for producing joints with acceptable properties in aluminum alloys and steels is the friction stir welding (FSW), which was developed at The Welding Institute (TWI), UK, in 1991 [1]. The FSW process has lower heat inputs than the conventional fusion welding reducing metallurgical changes in the heat affected zone (HAZ), does not produce gases or fumes, and can join materials that are difficult to fusion weld. Currently, this welding technique is used in various industries, such as aviation industry, automotive, railway manufacturing, and shipbuilding [2].

In the FSW process, as shown in Fig. 1(a), a non-consumable cylindrical tool with a profiled probe (pin) rotates and slowly plunges between two clamped plates until the tool shoulder touches the surface of the plates. The localized heating due to friction between the rotating shouldered tool and workpiece, and plastic deformation of the material softens the materials near the tool surfaces without reaching the melting point (a solid-state process). As the tool

traverses along the weld line, the plasticized material transfers from the front to the back of the tool pin. Since the local relative motion of the tool and the workpiece is a combination of the translational and rotational motions, the heat generation rate varies from one side to the other side of the workpiece, which are referred to as the advancing and retreating sides (Fig.1(b)). The temperature distribution directly affects the mechanical properties, the residual stress, the distortions, and the microstructure of the joints; therefore, it is important to predict the distribution of temperature during the FSW process.

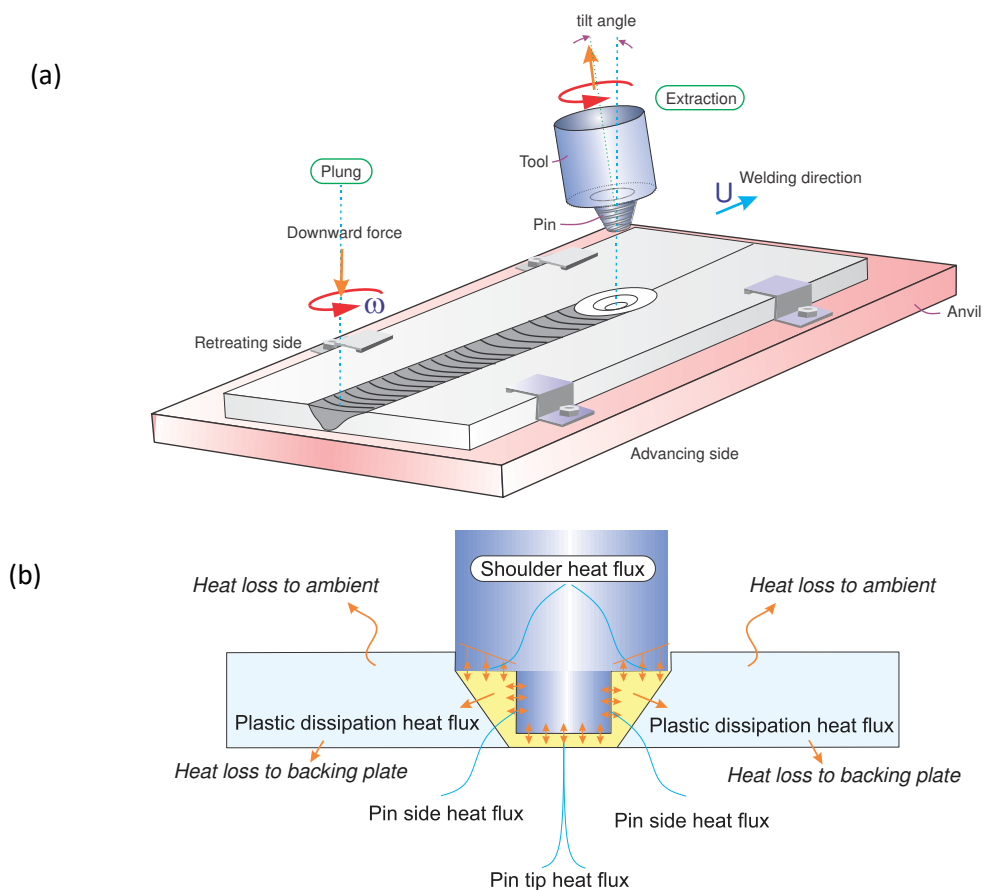


Fig.1. (a) Schematic diagram of the friction stir welding process and (b) the different heat generation regions.

Up to now, numerous models have been developed to simulate the heat transfer and materials flow during the FSW process. The nonlinear thermal equation can be solved either analytically or numerically for finding temperature variations during the FSW process. Vilaca et al. [3] developed an analytical thermal model to simulate the asymmetric temperature field

due to the combination of the translational and rotational motions of the welding tool in a FSW process. This model calculated the heat input by an iterative procedure referring to experimental data. Ferro and Bonollo [4] presented a semi-analytical thermal model for predicting the transient temperature profiles considering sticking between the tool/workpiece interfaces.

On the other hand, several authors simulated the FSW process numerically using the finite element method (FEM), computational fluid dynamics (CFD), or meshless methods. Darvazi et al. [5] used FEM analysis to calculate the thermal distribution and the residual stress difference at two sides of the weld line considering frictional heating and plastic deformation heating depended on both the temperature and the speed of the tool. Cho et al. [6] developed a three-dimensional thermo-mechanical model considering the phase transformation occurred during the FSW process using an Eulerian finite volume (FV) solver in the steady-state conditions. Fraser et al. [7] have recently presented an advanced meshfree computational framework using an innovative parallelization strategy on the graphics processing unit (GPU) to simulate the entire FSW process. Their simulation code allows determination of temperature, flow stresses, internal and surface defects.

In recent years, several authors have studied the temperature profile during the FSW process using a range of different numerical methods, which clearly indicates the importance of this research topic. Fagan et al. [8] presented a model for friction stir forming based on the material point method as a framework considering both plastic dissipation and frictional heating. They concluded this method could be used to predict the temperature profile and material flow with reasonable accuracy. Dialami et al. [9] presented a fully coupled thermo-mechanical model of the FSW process at global and local levels. In the global level approach,

they studied the effect of a moving heat source on the behavior of the entire workpiece, and in the local level approach, they analyzed the HAZ, and studied the heat source locally. Al-Moussawi et al. [10] developed a three-dimensional CFD model to simulate the FSW process in an Eulerian steady-state framework. Their model showed higher asymmetry in the temperature profiles for high welding speeds. Pei et al. [11] presented a selectively-coupled shear localization model which combined 3D transient heating and heat transport model with 1D shear localization model capable of estimating the FSW temperature profiles. Chen et al. [12] presented a three-dimensional simulation based on CFD to investigate the temperature distribution and deformation of the material in the FSW process. They employed different frictional boundary conditions in the CFD simulation to estimate their effects on behaviors of the temperature and material deformation.

The previous semi-analytical methods had some limitations, such as not considering all the components of heat generation, the temperature-dependent material properties, or the heat loss due to convection and radiation. In addition, the numerical methods are time-consuming, or are not applicable for later mechanical analysis; therefore, in the present paper, a semi-analytical thermal model is developed which considers all components of heat generation and heat loss due to convection and radiation, and can quickly and accurately predict the temperature distribution in the FSW process.

## **2. Mathematical modeling**

### *2.1. Governing equation*

The governing heat conduction equation for the transient heat transfer analysis during the FSW process is given as follows:

$$\rho C_p \frac{\partial T}{\partial t} = \frac{\partial}{\partial x} \left( k \frac{\partial T}{\partial x} \right) + \frac{\partial}{\partial y} \left( k \frac{\partial T}{\partial y} \right) + \frac{\partial}{\partial z} \left( k \frac{\partial T}{\partial z} \right) + Q_p \quad (1)$$

where  $\rho$ ,  $C_p$ , and  $k$  are the density, the specific heat capacity and the thermal conductivity of the material, respectively; the term  $Q_p$  is the volumetric heat generation caused by plastic dissipation in the FSW process. By removing  $Q_p$  from Eq. (1) and considering it as a surface flux boundary condition at the tool/workpiece interface, Eq. (1) can be simplified and then expanded as follows:

$$\rho C_p \frac{\partial T}{\partial t} = k \left( \frac{\partial^2 T}{\partial x^2} + \frac{\partial^2 T}{\partial y^2} + \frac{\partial^2 T}{\partial z^2} \right) + \frac{\partial k}{\partial T} \left( \left( \frac{\partial T}{\partial x} \right)^2 + \left( \frac{\partial T}{\partial y} \right)^2 + \left( \frac{\partial T}{\partial z} \right)^2 \right) \quad (2)$$

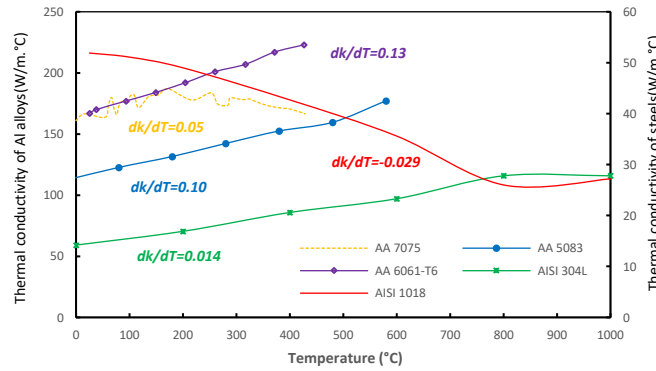


Fig.2. Thermal conductivity and its average slop versus temperature [13-17].

As shown in Fig. 2, the value of thermal conductivity does not significantly change with temperature [13-17], or  $\frac{\partial k}{\partial T} \approx 0$ . Thus, under the assumption of constant thermal properties, Eq. (2) can be reduced to a linear differential equation as follows:

$$\frac{1}{\alpha} \frac{\partial T}{\partial t} = \frac{\partial^2 T}{\partial x^2} + \frac{\partial^2 T}{\partial y^2} + \frac{\partial^2 T}{\partial z^2} \quad (3)$$

where  $\alpha = k / \rho c_p$  is the thermal diffusivity of the workpiece. In the theory developed by Rosenthal [18], a constant heat source is located at the origin of a rectangular coordinate

system moving at a constant speed with respect to the stationary rectangular coordinate system as shown in Fig. 3. Using this assumption and the relations shown in Fig. 3, Eq. (3) can be simplified as follows:

$$-\frac{v}{\alpha} \frac{\partial T}{\partial w} = \frac{\partial^2 T}{\partial w^2} + \frac{\partial^2 T}{\partial y^2} + \frac{\partial^2 T}{\partial z^2} \quad [4]$$

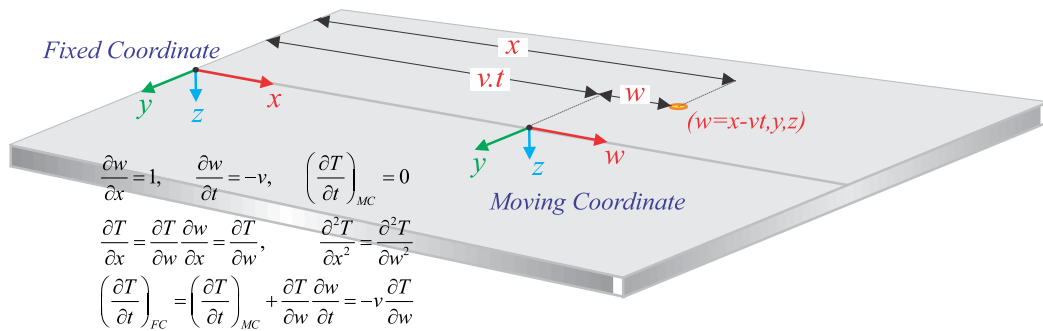


Fig. 3. Fixed general coordinate (FC) and steady-state moving coordinate (MC) in the FSW process.

The solution of Eq. (4) must satisfy the following conditions: 1) Since the source is a point source, the heat flux around the source must tend to the value of the total heat generation caused by both frictional and plastic deformation delivered to the workpiece, 2) There is no heat dissipation from the workpiece to the surrounding atmosphere, 3) The temperature of the workpiece remains unchanged at very great distance from the source. In addition, Eq. (4) is more easily handled by replacing it with the following expression derived from Appendix A:

$$T - T_0 = e^{-v.w/2\alpha} \phi(w, y, z) \quad (5)$$

Then, the final heat transfer governing equation becomes:

$$\frac{\partial^2 \phi}{\partial w^2} + \frac{\partial^2 \phi}{\partial y^2} + \frac{\partial^2 \phi}{\partial z^2} - (v/2\alpha)^2 \phi = 0 \quad (6)$$

Referring to Appendix B, the solution of Eq. (6) is provided for three-dimensional heat flows or thick plates in terms of the radial distance,  $R$ , from the heat source as follows:

$$T - T_0 = \frac{Q}{2\pi k} \frac{e^{-v(w+R)/2\alpha}}{R} \quad (7)$$

where  $Q$  is the total heat generation caused by both frictional and plastic deformation and also the plastic dissipation at a point source. For two-dimensional heat flows or thin plates, as described in Appendix C, the better results can be obtained by using the below equation:

$$T - T_0 = \frac{Q}{2\pi kH} e^{-\frac{v}{2\alpha}w} K_0\left(\frac{v}{2\alpha}r\right) \quad (8)$$

where  $H$  and  $K_0$  are the thickness of workpiece and the modified Bessel function of the second kind and zero order.

## 2.2. Heat generation

For modeling the heat generation in the FSW process, three contact states namely sticking, sliding, and partial sliding/sticking are considered. In the sticking or sliding condition, the material surface sticks, or slides to the moving tool surface, and the heat generation is produced by the plastic deformation or friction, respectively. In the mixed state, the heat is generated by both friction and plastic deformation in the shear layer. Using the definition of the tool rotational speed relative to surrounding materials (Fig. 4) and the mixed heat generation definition from the previous papers [14,19,20], the heat generation is formulated as follows:

$$q = q_{plastic} + q_{friction} = \frac{\sqrt{(k\rho c_p)_{WP}}}{\sqrt{(k\rho c_p)_{WP}} + \sqrt{(k\rho c_p)_{TP}}} (\eta\tau\delta + (1-\delta)\mu P)(\omega r - \psi v \sin \theta) \quad (9)$$

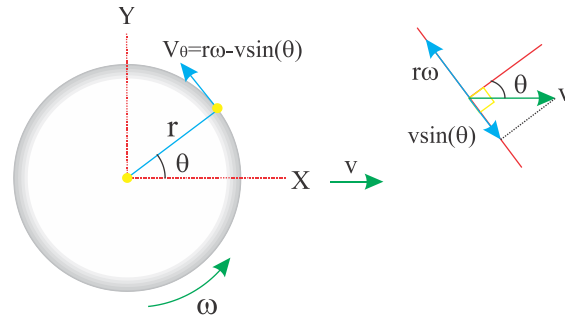


Fig. 4. The velocity of one point on the tool shoulder.

where  $\tau$ ,  $P$ ,  $\omega$ ,  $r$ ,  $\eta$ , and  $\mu$  are the shear yield stress of material, the normal pressure of the tool, the rotational speed of the tool, the radial distance of a point from the axis of the tool, the efficiency of process and the coefficient of friction, respectively; In Eq. (9),  $TP$  indicates the tool properties, and  $WP$  indicates the workpiece properties. In this paper, the shear yield stress (obtained by relation  $\tau = \sigma_{yield} / \sqrt{3}$ , where  $\sigma_{yield}$  is yield tensile stress) and friction coefficient are a function of temperature which are implemented in the model by means of a numerical routine.

In addition,  $\psi$  is the advancing retreating factor introduced by Darvazi et al. [24] and is about 20-30 in the present model, and  $\delta$  is the sticking state variable and is defined as the velocity of the contact points at the workpiece surface relative to the tool point in contact (sticking,  $\delta = 1$ ; sliding,  $\delta = 0$ ; and sticking/sliding,  $0 < \delta < 1$ )[16]. Finally, by substituting the total heat generation in Eqs. (7) and (8), in the case of 2D and 3D heat flow, and using the superposition principle, the temperature of the FSW process under the steady-state condition can be calculated.

### 2.3. Temperature rise in workpiece caused by the tool shoulder and the pin tip

The surface of the tool shoulder is divided along the radial and circumferential direction, as indicated in Fig. 5. The heat generation for an element positioned at point **A** can be determined by multiplying  $q$  with the area element in polar coordinates as follows:

$$dQ = qr \, dr \, d\theta \approx qr_i \Delta r \Delta \theta \quad (10)$$

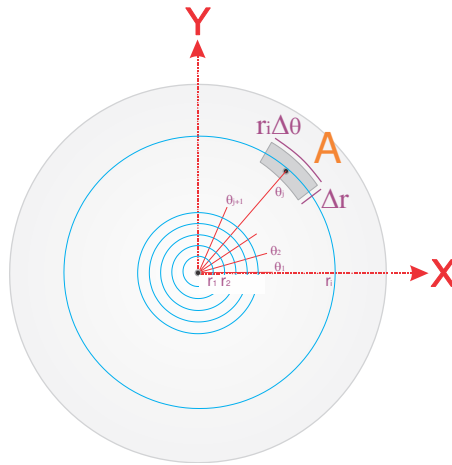


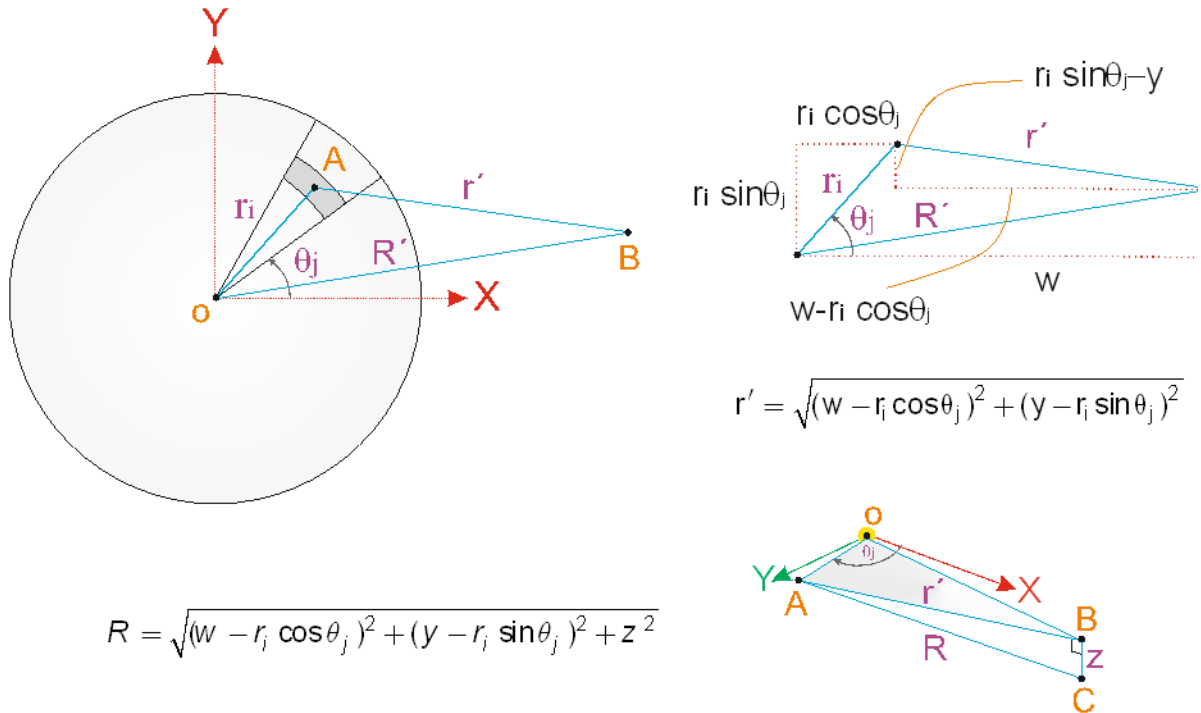
Fig. 5. Definition of an element on the surface of the tool shoulder.

where  $dQ$  is heat generation for an element substituting instead of  $Q$  in Eqs. (7) and (8), and  $q$  can be obtained from Eq.(9). As shown in Fig. 6, for an arbitrary point **C**, the heat generated at point **A** plays the role of heat source; therefore, the temperature generated by each element is described as follows:

$$T - T_0 = \frac{q}{2\pi k} \frac{e^{-\nu(R+w)/2\alpha}}{R} (r_i \Delta r \Delta \theta) \quad \text{for 3D heat flow (thick plates)} \quad (11)$$

$$T - T_0 = \frac{q}{2\pi k H} \left( e^{-\frac{\nu}{2\alpha} w} \right) K_0 \left( \frac{\nu}{2\alpha} r' \right) (r_i \Delta r \Delta \theta) \quad \text{for 2D heat flow (thin plates)} \quad (12)$$

where  $R$  and  $r'$  are the 3D and 2D distance from element center. The details of the calculation of these variables are given in Fig. 6.



$$R = \sqrt{(W - r_i \cos \theta_j)^2 + (y - r_i \sin \theta_j)^2 + z^2}$$

Fig. 6. The distance of one arbitrary point **C** from an element center.

Using the superposition principle and neglecting the nonlinearity effect of temperature in Eq. (2) and considering the 3D based model, the temperature induced by the tool shoulder in the steady-state condition can be calculated as follows:

$$\Delta T_{\text{shoulder}} = \frac{e^{-vw/2\alpha}}{2\pi k} \sum_{i=1}^n \sum_{j=1}^m q \frac{e^{-vR/2\alpha}}{R} r_i \Delta r \Delta \theta \quad (13)$$

where  $m$  and  $n$  are the number of divisions along the radial and circumferential directions, respectively. The temperature rise caused by the pin tip,  $\Delta T_{\text{pin tip}}$ , is calculated like the temperature rise caused by the shoulder.

#### 2.4. Temperature rise in workpiece caused by the pin side

As shown in Fig. 7, the temperature generated by the pin side is considered as 2D heat flow, and the total heat generation is calculated as follows:

$$dQ = qrH d\theta \approx q_r H \Delta \theta \quad (14)$$

where  $r_p$  is the radius of the pin of the tool. By substituting Eq. (14) in Eq. (12) for an element and integrating the effects of all elements, the temperature induced by the pin side in the steady-state condition can be calculated as follows:

$$\Delta T_{pin\ side} = \frac{e^{-\frac{v}{2\alpha}w}}{2\pi kH} \sum_{j=1}^m K_0\left(\frac{v}{2\alpha}r'\right) q r_p H \Delta\theta \quad (15)$$

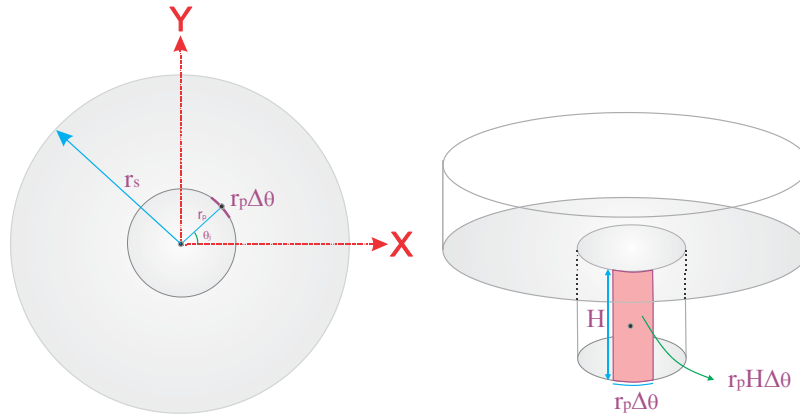


Fig. 7. Definition of an element on the pin side.

### 2.5. Temperature rise in workpiece due to plastic dissipation

The heat generated due to the plastic deformation dissipation away from the interfaces in the thermo-mechanically affected zone (TMAZ) is about 4.4% (0.044) of the total heat generation [14,20,21]. Avila (2006) [22] used an inverse trigonometric function, in order to better approximate the domain of TMAZ as illustrated in Fig. 8. The inverse tangent range is arbitrarily restricted to  $(-\pi/2, \pi/2)$ , and three constants are required to fit the function. The function used in this case is defined as follows:

$$Z = C_1 \left( \tan^{-1}(C_2 r_0 - 2\pi) + C_3 \right) \quad (16)$$

or

$$r_0 = \left( \tan\left(\frac{Z}{C_1} - C_3\right) + 2\pi \right) / C_2$$

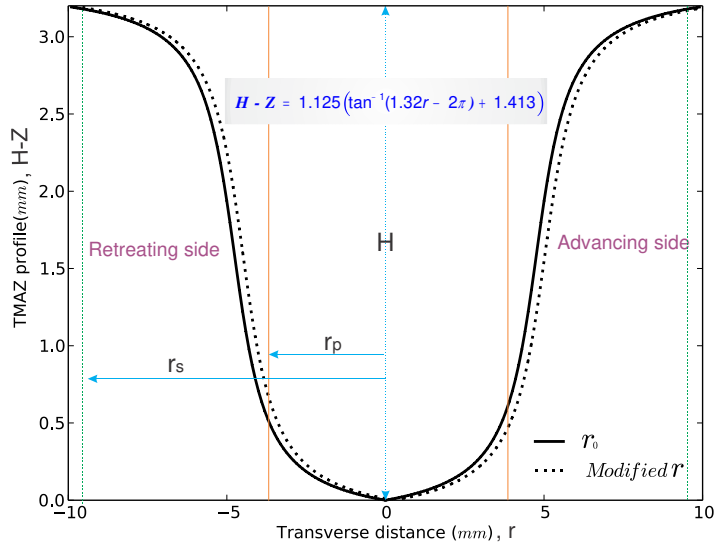


Fig. 8. The suggested TMAZ profile for 304L stainless steel at advancing and retreating side.

where all values of  $C1$ ,  $C2$ , and  $C3$  are constants depending on the tool dimensions in millimeters(mm). In the present study, the radius of the TMAZ is defined as  $R_{TMAZ} = r_0 - v / \omega \sin \theta$  which is wider at the advancing side than the retreating side as shown in Figs. 8 and 9. The heat generation in the TMAZ is estimated using Eq. (9) and neglecting the term of frictional heating; therefore, the heat generation due to plastic dissipation can be expressed as:

$$dQ_{TMAZ} = 0.044\eta\delta\tau(\omega R_{TMAZ} - v \sin \theta)R_{TMAZ} \Delta S \Delta \theta \quad (17)$$

where  $\Delta S$  is a line element on the TMAZ curve shown in Fig. 9 and can be approximated as follows:

$$\Delta S = \sqrt{\left(\frac{dZ}{dr}\right)^2 + 1} \Delta r \quad (18)$$

Then, the temperature rise due to plastic dissipation in the TMAZ region in an arbitrary point is calculated as follows:

$$\Delta T_{TMAZ} = \frac{e^{-vW/2\alpha}}{4\pi k} \sum_{i=1}^n \sum_{j=1}^m dQ_{TMAZ} \frac{e^{-vR/2\alpha}}{R} \quad (19)$$

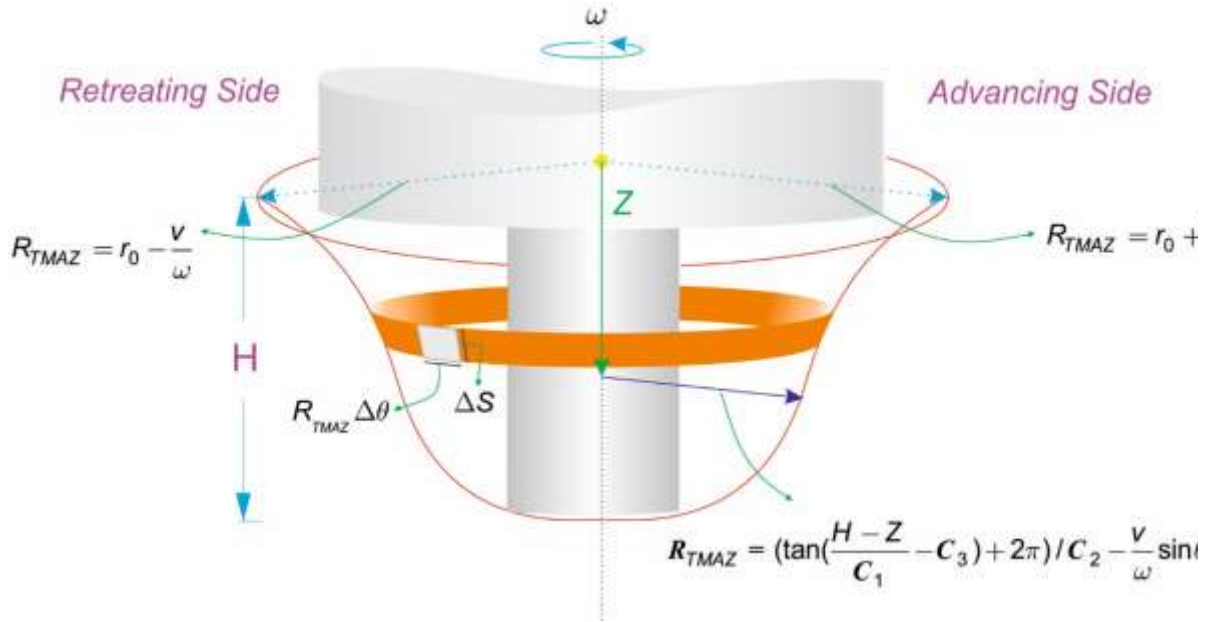


Fig. 9. The shape of the TMAZ and definition of its boundary.

## 2.6. Temperature change in workpiece due to convection from surfaces

Since the previous analytical models had not considered the heat loss due to convection and radiation, the estimated temperature almost would be higher than the actual value. For solving this problem, two methods can be used. First, the temperature distribution can be multiplied by a factor to correlate the temperature results from the semi-analytical method and experimental results. The second method considers the heat loss due to convection and radiation as a heat sink and is defined as Eq. (20).

As shown in Fig. 10, the workpiece is divided along the x and y directions, and the distance between the heat source (the point **B**) and an arbitrary point (point **A**),  $R$ , is calculated; then the temperature drop of point **A** due to convection and radiation is calculated using Eq. (9) as follows:

$$dQ_C = -(h(T - T_0) + \varepsilon\beta(T^4 - T_0^4))\Delta x \Delta y \quad (20)$$

$$\Delta T_{Top-con-rad} = \frac{e^{-\nu w / 2\alpha}}{2\pi k} \sum_{i=1}^n \sum_{j=1}^m dQ_C \frac{e^{-\nu R_C / 2\alpha}}{R_C} \Delta x \Delta y \quad (21)$$

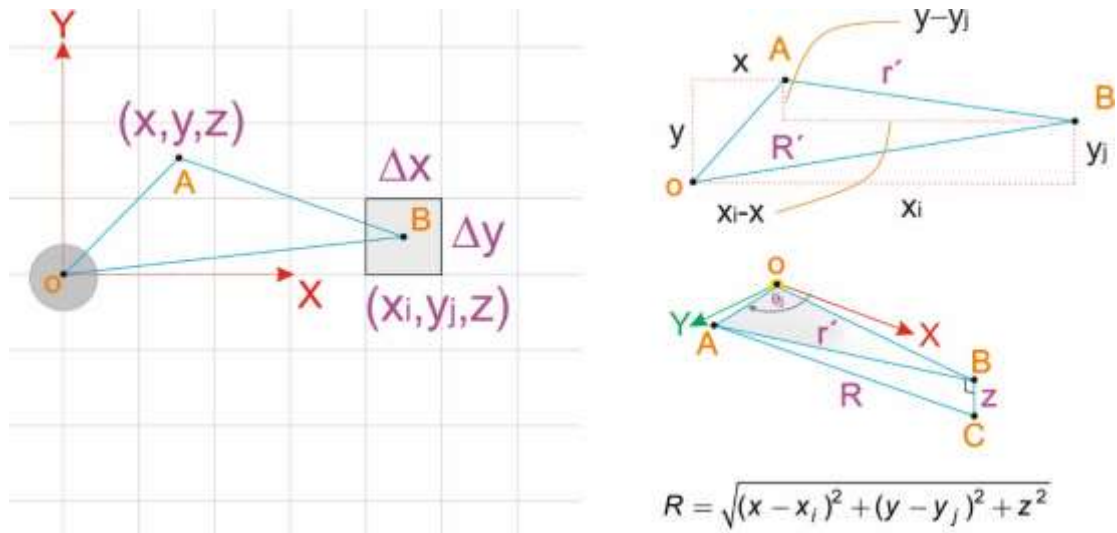


Fig. 10. Modeling of heat loss due to convection and radiation as a heat sink at the top surface.

where  $T_0$  is the ambient or initial temperature (22-25°C);  $h$  is the convection coefficient;  $\varepsilon$  is the surface radiation emissivity; and  $\beta$  is the Stefan-Boltzmann constant. Furthermore, the surface of the workpiece in contact with the backing plate is modeled as a convection condition with a higher convection coefficient, and the temperature drop due to it,  $\Delta T_{bottom-con}$ , is calculated using Eqs. (20) and (21) without considering the radiation condition, and  $Z$  is replaced by  $H-Z$ . The implementation of Eq. (21) needs to use a routine for reaching a steady-state condition.

### 2.7. Finding total temperature distribution

In Eq.(2) the terms of nonlinearity are removed, and it is reduced to a linear differential equation. According to the superposition principle, which is correct for linear equations, the resultant effect is the sum of the effects produced by each component acting separately; therefore, the total temperature distribution can be calculated by Eq. (22). The temperature distributions for aluminum alloy 5083-H118 are shown in 3D views in Fig. 11, which is

calculated using the present model through a numerical code written in FORTRAN programming language.

$$T_{Total} = T_0 + \Delta T_{shoulder} + \Delta T_{TMAZ} + \Delta T_{pin\ side} + \Delta T_{pin\ tip} + \Delta T_{top-con-rad} + \Delta T_{bottom-con} \quad (22)$$

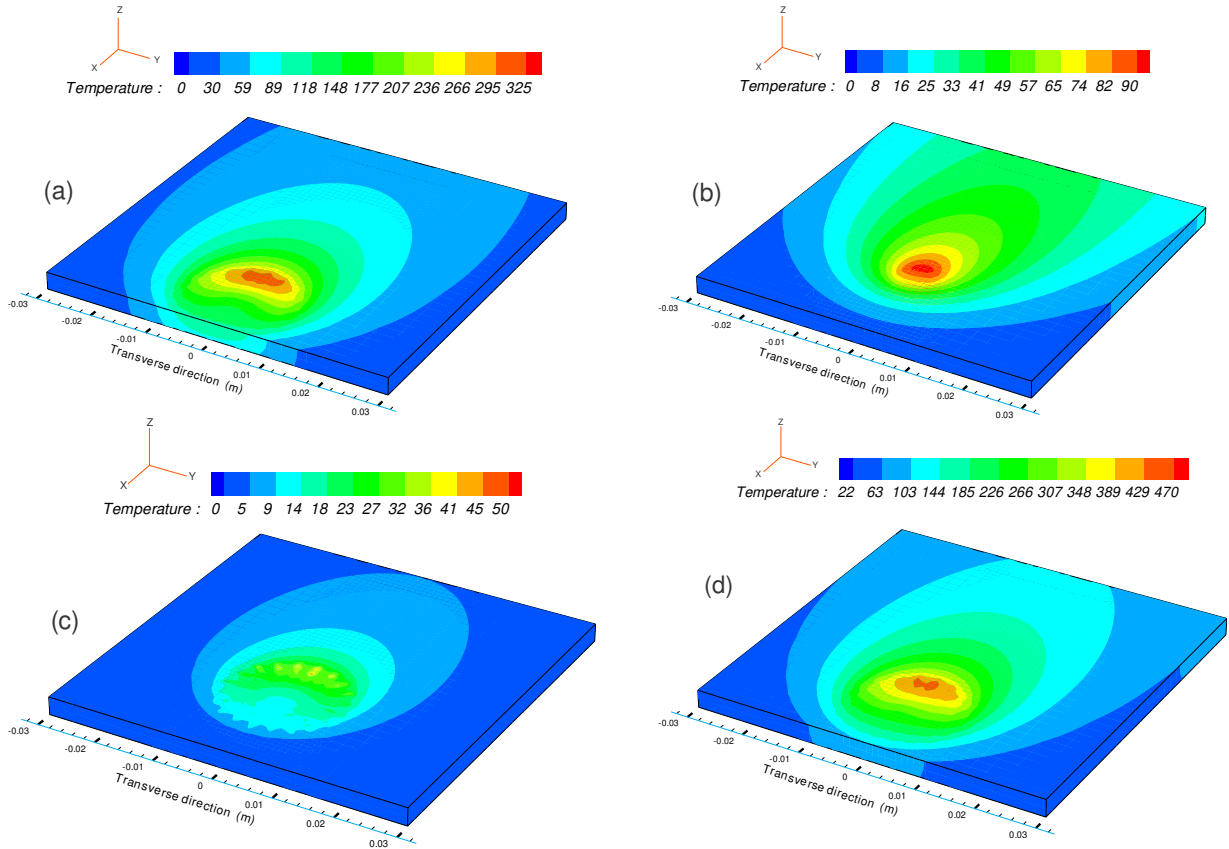


Fig. 11. The distribution of temperature for AA5083-H118 calculated via the present semi-analytical model induced by (a) the shoulder, (b) the pin, (c) the plastic dissipation in TMAZ and (d) total temperature for the welding condition of 800 rpm and 30 mm/min.

The maximum temperature occurs at the location with  $w$  equal to zero; in this point, the temperature distribution function is singular. In this paper, two methods are used for handling this singularity. In cases that the maximum temperature is unknown, only the part of the model is simulated in which  $R$  is not zero. In cases that the maximum temperature is known,  $R+\varepsilon$  is used instead of  $R$ , and the following relation is applied for finding the appropriate value of  $\varepsilon$ :

$$\lim_{R \rightarrow 0} T = T_{max} \Rightarrow \varepsilon = \varepsilon_0 \quad (23)$$

### 3. Materials and experimental procedure

In the present paper, the temperature-dependent thermal and mechanical properties of the material such as specific heat, thermal conductivity, density and yield shear stress are taken from the previous literature [13-17,23]. A numerical routine is constructed to determine the temperature-dependent thermal properties during the analysis. At the beginning of the analysis, the material properties at the ambient temperature are implemented to the model, and the temperature is calculated by Eq.(22); then using the previous temperature distribution, the material properties are updated and applied to the model estimating the new temperature distribution. This process is repeated sequentially until a steady-state temperature distribution is achieved. The schematic of temperature updating is shown in Fig.

12.

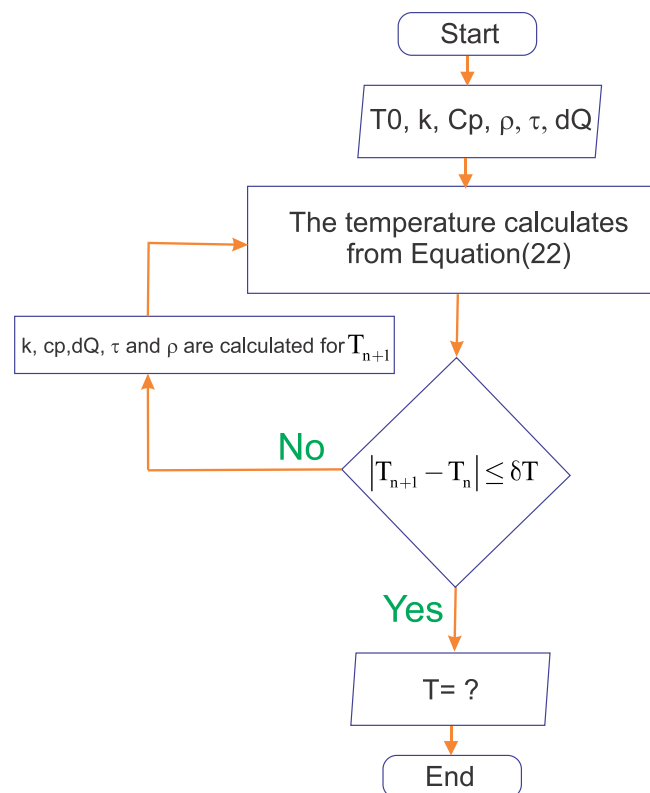


Fig.12. The algorithm of the numerical code for material updating written in Fortran language (in the present paper  $\delta T=1^{\circ}\text{C}$ ).

The accuracy of the present model is verified by comparing to already existing experimental results from the available literature (Zhu and Chao [13] for AISI 304L, lienert et al. [24] for AISI 1018, Song and Kovacevic [25] for AA 6061-T6 and, Colegrove and Shercliff [23] for AA7075-T7351). Furthermore, in order to validate the thermal histories of the AA5083-H118 base material, supplied in 3 mm thick plates welded by the FSW process, the experimental process is installed. Friction stir welding is carried out on a CNC vertical milling machine. In the experiments, the thermal histories on surfaces are measured using K-type thermocouples located at different distances from the weld line, as shown in Fig. 13. The data used for the calculations such as tool geometry and welding conditions are presented in Table I.

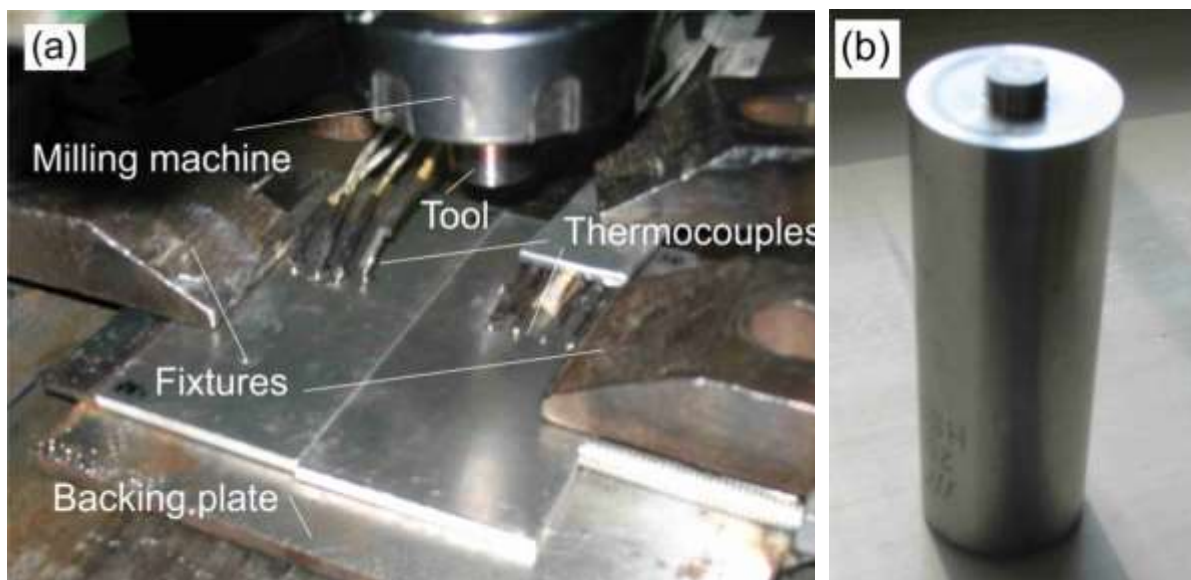


Fig. 13. Experimental installation (a) workpiece and thermocouple installation and (b) the Tool geometry.

**Table I.** The data used in the simulation of FSW process of aluminum alloys and steels.

Property/ Material	AISI 304L	AISI 1018	AA5083-H118	AA6061-T6	AA7075-T7351
Shoulder diameter, mm	19.05	19.0	20	50	23
Pin diameter, mm	6.35	7.9	6	12	8 to 10.2
Rotational speed, rpm	300 to 500	450	800 to 1400	1400	220 to 457
Welding speed, mm/min	102	25	100	100	220 to 457
Plate thickness, mm	3.18	6.35	3	12.7	6.35
Tool material	tungsten alloys	molybdenum and tungsten alloys	HS - tool steel	HS - tool steel	HS - tool steel
Friction coefficient	0.78(25°C) to 0.0 (1450°C)	0.78 to 0	0.4 to 0	0.4 to 0	0.4 to 0
Axial pressure, MPa	109	69.5	8 to 12	12.7	6
Heat transfer coefficient to ambient, h	0.0668T (T≤500°C), 0.231T -82.1(T>500°C)	15 to 30	30	30	30
Backing plate heat transfer coefficient	10h	50	200 to 2000	350 to 1000	350 to 1000

<b>Melting point</b>	1400 -1450°C	1420 -1460°C	591-638°C	582 - 652°C	477-635°C
<b>Material References</b>	Zhu and Chao [13]; Darvazi et al. [5]; Nandan et al. [20]	Nandan et al. [14]; Lienert et al.[24]	Kim et al. [17]	Nandan et al. [16]; Song and Kovacevic [25]	Touloukian et al. [15]; Colegrove and Shercliff [23]

---

## 4. Results and verifications

### 4.1. Friction stir welding of 304L stainless steel

The temperature distribution of 304L stainless steel is calculated and compared with the experimental results of Zhu and Chao [13]. To maintain consistency, the material properties, the diameter of the shoulder and pin, the pin length, the rotational and translational speeds are considered the same as the previous paper. The variations of temperature from the semi-analytical method and from measurement against time history at the middle of the workpiece at the thermocouple locations of 18, 21, and 26.5 mm from the weld line are shown in Fig. 14 for the rotational speed of 300 rpm. In addition, Fig. 15 compares the variations of the temperature on the top surface at the locations of 17, 21, and 25 mm for the rotational speed of 500 rpm. The comparisons show that the results of the present model are in good agreement with the experimental data, and the present model is suitable for thermal analysis of 304L stainless steel.

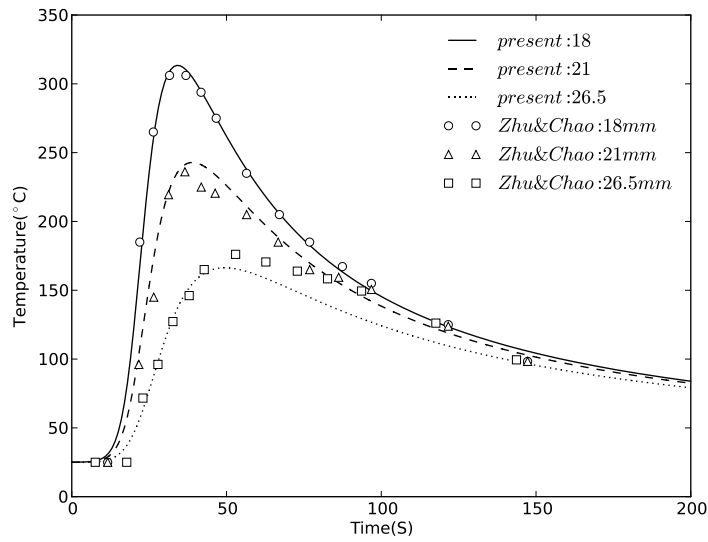


Fig. 14. Comparison between the experimental data [13] and calculated temperature histories on the top of the retreating side of the workpiece at various distance from the weld line for the translational speed of 102 mm/min and the rotational speed of 300 rpm.

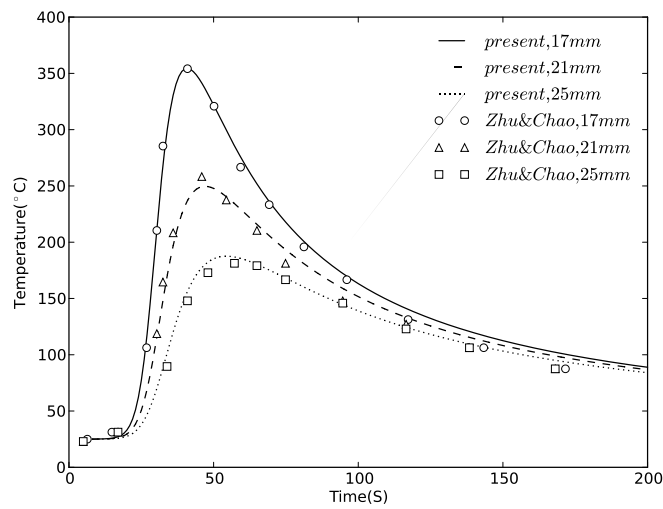


Fig. 15. Comparison between the experimental data [13] and calculated temperature histories on the top of the retreating side of the workpiece at various distance from the weld line for the translational speed of 102 mm/min and the rotational speed of 500 rpm.

#### 4.2. Friction stir welding of Mild steel 1018

The calculated temperature history on the advancing side at a distance of 12.7 mm from the weld line is compared with the experimental data [24] in Fig. 16. A good agreement between the calculated and measured results indicates that the developed model can be used for the prediction of temperature profiles and cooling rates.

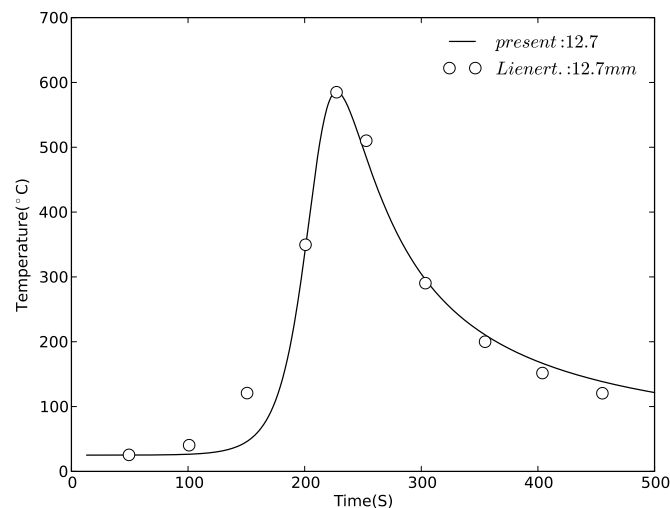


Fig. 16. Comparison between the experimental [24] and calculated temperature histories on the advancing side at a point 12.7 mm from the weld line for the translational speed of 25 mm/min and the rotational speed of 450 rpm.

#### 4.3. Friction stir welding of aluminum alloy 5083-H118

Another verification of the proposed model is carried out by comparison with the experimental measurements. The welding parameters associated with the three different FSW conditions are presented in Table I. The thermocouples are inserted into holes with a depth of 1 mm from the top surface at a distance of 15, 21 and 32 from the welding centerline. The comparison of the calculated temperature histories and the experimental data shows good agreement between them (Figs. 17, 18, and 19).

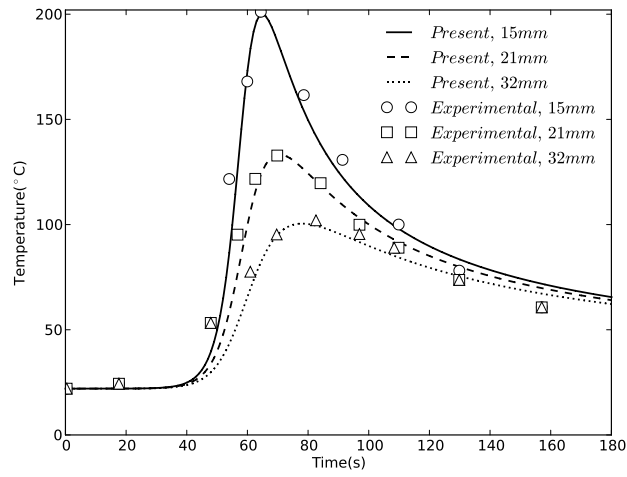


Fig. 17. The temperature histories at various distance from the weld line for the rotational speed of 800 rpm and the translational speed of 100 mm/min.

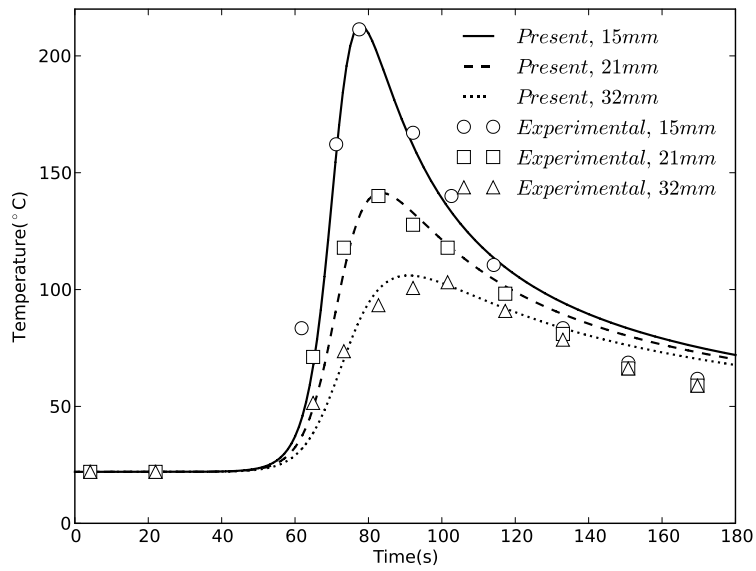


Fig. 18. The temperature histories at various distance from the weld line for the rotational speed of 1100 rpm and the translational speed of 100 mm/min.

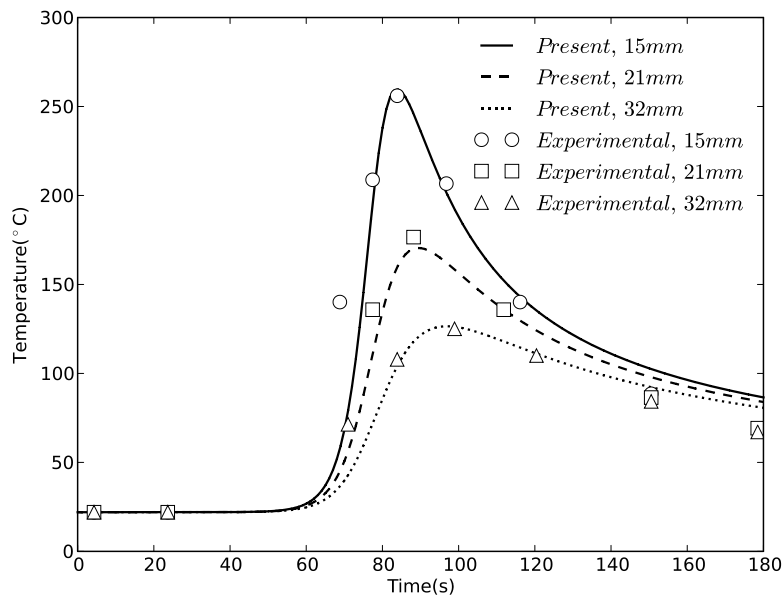


Fig. 19. The temperature histories at various distance from the weld line for the rotational speed of 1400 rpm and the translational speed of 100 mm/min.

#### 4.4. Friction stir welding of aluminum alloy 6061-T6

The calculated temperature histories at two locations are compared with the experimental data from the literature [25] in Fig. 20. Good agreements between the experimentally determined and the numerically calculated results at two locations indicate that the model can be used to examine the temperature profiles and cooling rates.

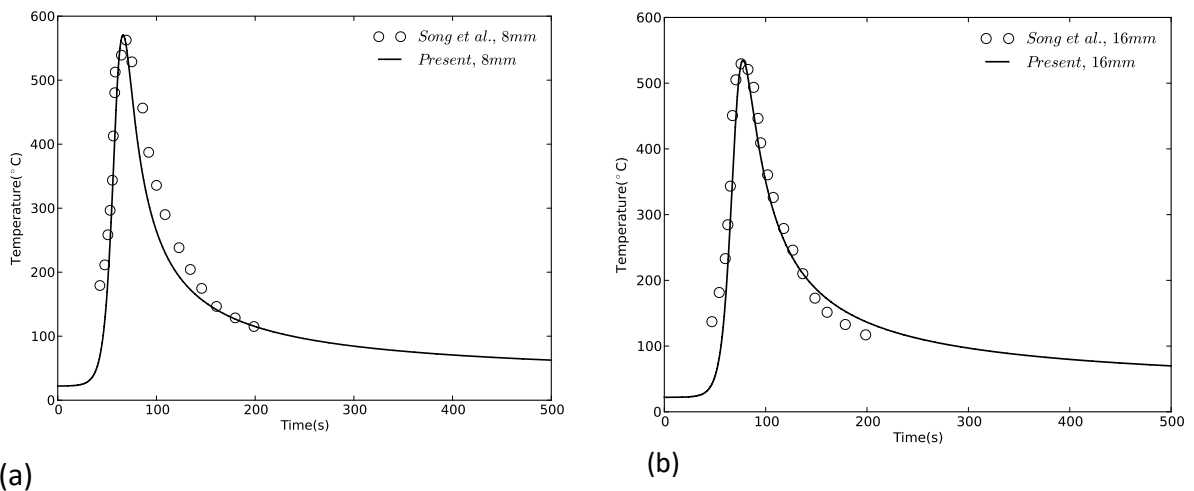


Fig. 20. Comparison between the experimental [25] and calculated temperature histories at points 2 mm below the top surface at a distance of ( a ) 8 mm and ( b ) 16 mm from the centerline for the rotational speed of 1400 rpm and the translational speed of 100 mm/min.

#### 4.5. Aluminum alloy 7075-T7351

In order to verify the model, the calculated temperature variations are compared with the experimental data from Colegrove and Shercliff [23] that were obtained using thermocouples at various locations, as shown in Fig. 21. The calculated results match very closely with the experimental data.

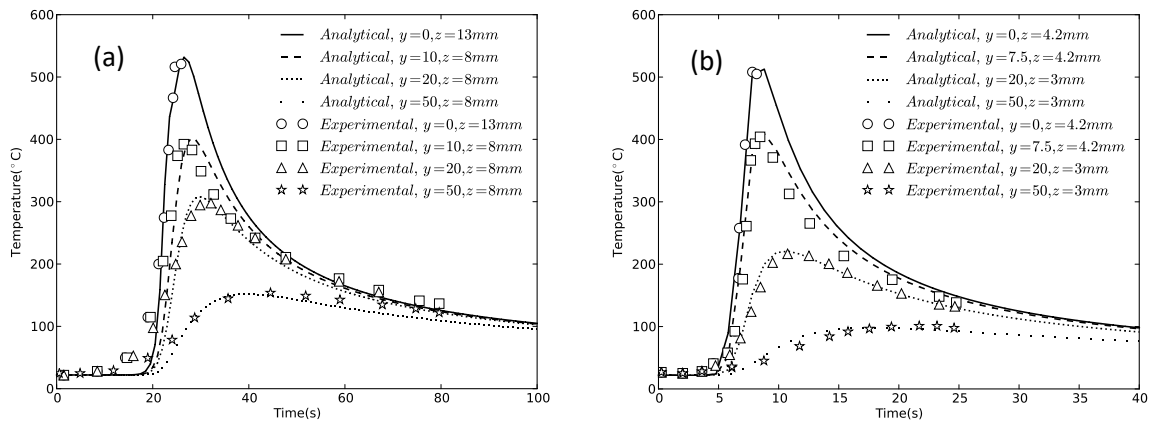


Fig. 21. Comparison between the experimental [23] and calculated temperature histories at different locations for welding conditions of (a) 220 rpm and 220 mm/min, and (b) 457 rpm and 457 mm/min.

### 5. Discussion

The temperature distribution has been calculated by a semi-analytical method, as shown in Fig. 22. The heat-generating regions are divided into many elements that each element is considered as a heat source, and for an arbitrary point C, the heat generated at point  $A_n$  plays the role of a heat source (Fig. 22). Finally, the temperature distribution is calculated by integrating the effects of each heat source.

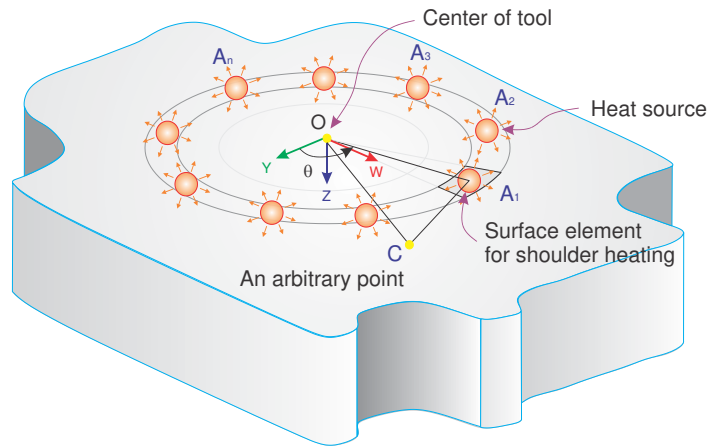


Fig.22. Schematic of any element of the shoulder region as a heat source.

As proposed by previous researchers [4] the heat source can be considered to be concentrated at the mid thickness of the workpiece in the center of the nugget and traveling with a constant linear velocity ( $v$ ) (Fig. 23(a)), whereas in the presented model as shown in Fig. 23(b), the heat sources are distributed in all regions where the heat is generated. They also used the constant thermal properties at the ambient temperature, and did not consider the heat radiation or convection and backing plate in temperature calculation.

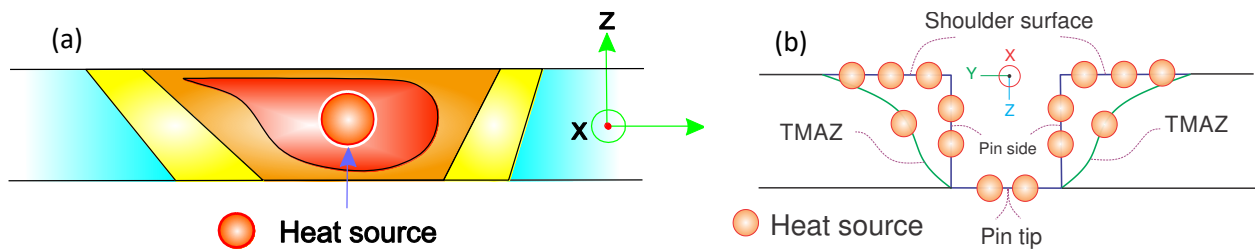


Fig.23. Modeling of heat source: (a) the Ferro and Bonollo model [4] and (b) the present model.

Figs. 24 (a) through (d) show the temperature profiles on the top surface computed by the present semi-analytical method and previous numerical methods. In Fig. 24(a), the temperature distribution was calculated by a commercial CFD code, FLUENT, based on a 3D viscoplastic model [26], and in Figs. 24(b) and (c) the temperature was calculated by FE method based on solid mechanics heat transfer model [20,27]. As shown in Fig. 24(d), the present model can also predict the temperature distribution like the previous methods;

however, it shows that the temperature distribution is asymmetric around the weld line, and the maximum temperatures are found in the back half of the shoulder/workpiece interface and toward advancing side. In comparison with the CFD and FE methods, the present method is time effective, and converges quickly, so it can be useful for the parametric study of the FSW process.

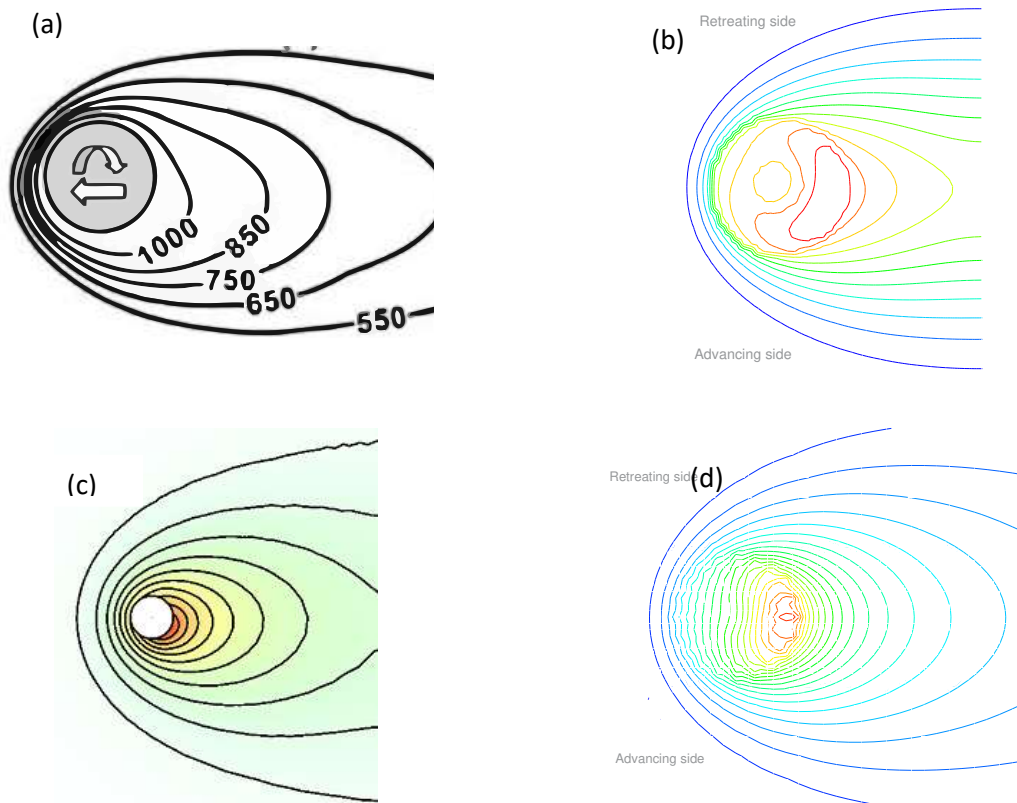


Fig. 24. The Computed temperature profiles on the top surface of workpiece for the rotational speed of 300 rpm and the translational speed of 102 mm/min: (a) Nandan et al. [26], (b) Darvazi et al. [20], (c) He et al. [27] and (d) The present work.

Figs. 25(a) and (b) show the cross-sectional temperature distribution of the FSW process in the transverse direction computed by Darvazi et al. [20] and the present model. The comparison shows that the present model can predict the thermal regions, and the hot zone is toward the advancing side. In addition, to highlight the characteristics of the proposed model, comparisons are made with the experimental data for various metals as shown in Figs. 14 through 21. The comparisons show that the results of the present model are in good

agreement with the experimental data, and the present model is suitable for thermal analysis of metals.

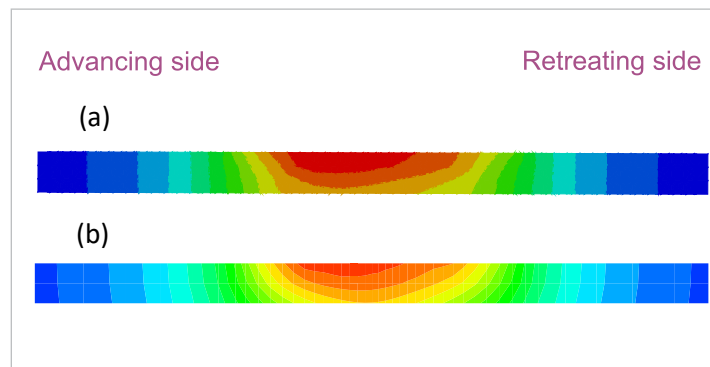


Fig.25. The cross-sectional temperature distribution of the FSW in the transverse direction computed by: a) Darvazi et al. [20] and b) the present method.

Although the temperature-dependent thermal conductivity and diffusivity are implemented during the analysis, they are considered constant with temperature for each element (point heat source) in Eq. (2) and (3). This limitation causes some differences between the calculated results and the experimental data in the low-temperature zone, and these differences decrease in the high-temperature zone in which the metals exhibit an almost constant thermal conductivity and diffusivity behaviors (Figs. 13 through 20). Furthermore, this method can be used for additional studies about friction stir welding, which includes thermal cycles or thermal distribution and can be used for mechanical analysis such as thermal stress during the welding process.

## 6. Conclusions

A semi-analytical model for prediction of temperature distribution has been developed and validated for various steel and aluminum alloys such as AISI 1018, AISI 304L, AA5083-H118, AA6061-T6, and AA7075-T7351. The main advantages of the present model in relation to other techniques for calculating the temperature are that:

- It considers main components of heat generation, such as friction and plastic deformation heat generation at the shoulder and pin sides, and plastic dissipation heating in thermo-mechanically affected zone.
- The heat loss due to convection and radiation at the top surfaces, and convection at the backing plate are considered in the model.
- The temperature-dependent material properties are updated by a numerical routine as temperature changes.
- This method predicts the asymmetric temperature at the advancing and retreating sides.
- Since this method considers the most parameters of the FSW process, it is suitable for studying the parameters affecting the temperature distribution.
- The present method is fast and accurate enough for predicting temperature distribution and is applicable for later mechanical analysis.

## APPENDIX A: Finding the form of solution

By considering the solution of Eq. (4) as a product of two separate functions given by:

$$T - T_0 = f(w) \phi(w, y, z) \quad (\text{A.1})$$

Eq. (4) converts to the following equation:

$$f \cdot (\phi_{ww} + \phi_{yy} + \phi_{zz}) + \left( 2f_w + \frac{v}{\alpha} f \right) \phi_w + \left( f_{ww} + \frac{v}{\alpha} f_w \right) \phi = 0 \quad (\text{A.2})$$

By assuming that the variable coefficient of term involving  $\phi_w$  is equal to zero, Eq. (A.2) converts to the homogeneous modified Helmholtz equation, and then the function  $f$  can be calculated:

$$2f_w + \frac{v}{\alpha} f = 0 \quad \Rightarrow \quad f = e^{-\frac{v}{2\alpha} w} \quad (\text{A.3})$$

## APPENDIX B: Three-dimensional solution

Eq.(6) in spherical coordinate in the quasi-stationary state can be expressed as follows:

$$\frac{1}{R^2} \left( \frac{\partial}{\partial R} \left( R^2 \frac{\partial \emptyset}{\partial R} \right) \right) - \left( \frac{v}{2\alpha} \right)^2 \emptyset = 0 \quad (\text{B.1})$$

By using  $\emptyset = \frac{u}{R}$ , Eq. (B.1) can be simplified as below:

$$\frac{\partial^2 u}{\partial R^2} - \left( \frac{v}{2\alpha} \right)^2 u = 0 \quad (\text{B.2})$$

The solution of Eq. (B.2) is:

$$u = A e^{-\frac{v}{2\alpha} R} + B e^{\frac{v}{2\alpha} R} \quad (\text{B.3})$$

By implementing the condition:

I) The temperature of the workpiece remains unchanged at infinite distance from the source, i.e.:

$$R \rightarrow \infty \quad |u| = \infty \text{ (or } T = T_0) \Rightarrow B = 0 \quad (\text{B.4})$$

Then Eq. (5) becomes:

$$T - T_0 = e^{-\left(\frac{v}{2\alpha}\right)R} \emptyset = e^{-\left(\frac{v}{2\alpha}\right)R} \frac{u}{R} = A e^{-\left(\frac{v}{2\alpha}\right)R} \frac{e^{-\left(\frac{v}{2\alpha}\right)R}}{R} \quad (\text{B.5})$$

II) The heat flux through the surface of the hemisphere drawn around the source must tend to the value of the total heat, Q, delivered to the workpiece, as the radius of sphere tends to zero:

$$\lim_{R \rightarrow 0} \left( -2\pi R^2 k \frac{\partial T}{\partial R} \right) = Q \quad (\text{B.6})$$

$$\lim_{R \rightarrow 0} \left( -2\pi R^2 k A \left( \frac{e^{-\frac{v}{2\alpha}(R+w)}}{-R^2} + \frac{e^{-\frac{v}{2\alpha}(R+w)}}{R} \left( -\frac{v}{2\alpha} \right) \left( 1 + \frac{R}{w} \right) \right) \right) = Q \Rightarrow A = \frac{Q}{2\pi k} \quad (\text{B.7})$$

where  $R = \sqrt{w^2 + y^2 + z^2}$ , and  $\frac{\partial w}{\partial R} = \frac{R}{w}$ .

In addition, when the heat source is volumetric, such as that in the TMAZ region, the heat flux diffuses radially in a spherical shape (not hemisphere), and the Eq. (B.6) should be rewritten as follows:

$$\lim_{R \rightarrow 0} \left( -4\pi R^2 k \frac{\partial T}{\partial R} \right) = Q \Rightarrow A = \frac{Q}{4\pi k} \quad (\text{B.8})$$

### APPENDIX C: Two-dimensional solution

Eq. (6) in cylindrical coordinate in the quasi-stationary state can be expressed as follows:

$$\frac{1}{r} \left( \frac{\partial}{\partial r} \left( r \frac{\partial \emptyset}{\partial r} \right) \right) - \left( \frac{v}{2\alpha} \right)^2 \emptyset = 0 \quad (\text{C.1})$$

The solution of the above Bessel equation is:

$$\varnothing = CI_0\left(\frac{vr}{2\alpha}\right) + DK_0\left(\frac{vr}{2\alpha}\right) \quad (\text{C.2})$$

$$\text{where } r \rightarrow \infty \quad |\varnothing| = \infty \Rightarrow C = 0 \quad \left( \text{because : } \lim_{x \rightarrow \infty} (I_0(x)) = \infty \right) \quad (\text{C.3})$$

$$T - T_0 = e^{-(v/2\alpha)w} \varnothing = De^{-\frac{v}{2\alpha}w} K_0\left(\frac{vr}{2\alpha}\right) \quad (\text{C.4})$$

The boundary condition must be satisfied as follows:

$$\lim_{r \rightarrow 0} \left( -2\pi r H k \frac{\partial T}{\partial r} \right) = Q \quad (\text{C.5})$$

Using the derivative identities of Bessel functions:

$$\frac{\partial K_0(x)}{\partial x} = -K_1(x) \quad (\text{C.6})$$

Eq. (C.5) expanded as follows:

$$\lim_{r \rightarrow 0} \left( -2\pi r H k D \left( -\frac{v}{2\alpha} K_1\left(\frac{vr}{2\alpha}\right) e^{-\frac{v}{2\alpha}w} + K_0\left(\frac{vr}{2\alpha}\right) e^{-\frac{v}{2\alpha}w} \left( -\frac{v}{2\alpha} \right) \left( \frac{\partial w}{\partial r} \right) \right) \right) = Q \quad (\text{C.7})$$

$$\text{where } r = \sqrt{w^2 + y^2} \quad \text{and} \quad \frac{\partial w}{\partial r} = \frac{r}{w}.$$

For small arguments  $x \ll n$ ,  $K_n(x)$  becomes, asymptotically, simple powers of its argument [28]:

$$K_n(x) \approx \frac{(n-1)!}{2} \left( \frac{x}{2} \right)^{-n} \quad n > 0 \quad (\text{C.8})$$

$$K_1 \approx \frac{(0)!}{2} \left( \frac{vr}{4\alpha} \right)^{-1} = \frac{2\alpha}{vr} \quad n > 0 \quad (\text{C.9})$$

By substituting Eq. (C.9) in Eq. (C.7) and tending  $r$  to zero, the constant D can be determined as:

$$D = \frac{Q}{2\pi k H} \quad (\text{C.10})$$

## **Declarations**

**Funding:** Not applicable

**Conflicts of interest/Competing interests:** The authors disclose that they do not have any competing interests.

**Availability of data and material:** Not applicable

**Code availability:** Not applicable

**Authors' contributions:** Not applicable

**Ethics approval:** This manuscript has not been simultaneously submitted to another journal for review. The work submitted is original and has never been published in any form or language before (partially or in full).

**Consent to participate:** Not applicable

**Consent for publication:** Not applicable

## References

1. Thomas WM, Nicholas ED, Needham JC, Murch MG, Temple-Smith P, Dawes CJ (1991) Friction stir butt welding. International Patent Application No.PCT/GB92102203 and Great Britain Patent Application No. 9125978.8,
2. Çam G, İpekoğlu G, Küçükömeroğlu T, Aktarer S (2017) Applicability of friction stir welding to steels. *Journal of Achievements in Materials and Manufacturing Engineering* 80 (2)
3. Vilaça P, Quintino L, dos Santos JF (2005) iSTIR—Analytical thermal model for friction stir welding. *Journal of Materials Processing Technology* 169 (3):452-465.  
doi:<https://doi.org/10.1016/j.jmatprotec.2004.12.016>
4. Ferro P, Bonollo F (2010) A semianalytical thermal model for friction stir welding. *Metall and Mat Trans A* 41 (2):440-449. doi:10.1007/s11661-009-0104-y
5. Darvazi AR, Iranmanesh M (2014) Prediction of asymmetric transient temperature and longitudinal residual stress in friction stir welding of 304L stainless steel. *Materials & Design* 55:812-820. doi:<https://doi.org/10.1016/j.matdes.2013.10.030>
6. Cho H-H, Kim D-W, Hong S-T, Jeong Y-H, Lee K, Cho Y-G, Kang SH, Han HN (2015) Three-Dimensional Numerical Model Considering Phase Transformation in Friction Stir Welding of Steel. *Metall and Mat Trans A* 46 (12):6040-6051. doi:10.1007/s11661-015-3177-9
7. Fraser K, Kiss L, St-Georges L, Drolet D (2018) Optimization of Friction Stir Weld Joint Quality Using a Meshfree Fully-Coupled Thermo-Mechanics Approach. *Metals* 8 (2):101
8. Fagan T, Lemiale V, Nairn J, Ahuja Y, Ibrahim R, Estrin Y (2016) Detailed thermal and material flow analyses of friction stir forming using a three-dimensional particle based model. *Journal of Materials Processing Technology* 231:422-430. doi:<https://doi.org/10.1016/j.jmatprotec.2016.01.009>
9. Dialami N, Chiumenti M, Cervera M, Agelet de Saracibar C (2017) Challenges in Thermo-mechanical Analysis of Friction Stir Welding Processes. *Archives of Computational Methods in Engineering* 24 (1):189-225. doi:10.1007/s11831-015-9163-y
10. Al-moussawi M, Smith AJ, Young A, Cater S, Faraji M (2017) Modelling of friction stir welding of DH36 steel. *The International Journal of Advanced Manufacturing Technology* 92 (1):341-360. doi:10.1007/s00170-017-0147-y
11. Pei X, Dong P (2017) A selectively-coupled shear localization model for friction stir welding process window estimation. *International Journal of Machine Tools and Manufacture* 123:89-104. doi:<https://doi.org/10.1016/j.ijmachtools.2017.08.003>
12. Chen G, Ma Q, Zhang S, Wu J, Zhang G, Shi Q (2018) Computational fluid dynamics simulation of friction stir welding: A comparative study on different frictional boundary conditions. *Journal of Materials Science & Technology* 34 (1):128-134. doi:<https://doi.org/10.1016/j.jmst.2017.10.015>
13. Zhu XK, Chao YJ (2004) Numerical simulation of transient temperature and residual stresses in friction stir welding of 304L stainless steel. *Journal of Materials Processing Technology* 146 (2):263-272. doi:<http://dx.doi.org/10.1016/j.jmatprotec.2003.10.025>
14. Nandan R, Roy GG, Lienert TJ, Debroy T (2007) Three-dimensional heat and material flow during friction stir welding of mild steel. *Acta Materialia* 55 (3):883-895.  
doi:<http://dx.doi.org/10.1016/j.actamat.2006.09.009>
15. Touloukian Y, Powell R, Ho C, Klemens P (1970) Thermophysical properties of matter-the tprc data series. volume 1. thermal conductivity-metallic elements and alloys. THERMOPHYSICAL AND ELECTRONIC PROPERTIES INFORMATION ANALYSIS CENTER LAFAYETTE IN,
16. Nandan R, Roy GG, Debroy T (2006) Numerical simulation of three-dimensional heat transfer and plastic flow during friction stir welding. *Metall and Mat Trans A* 37 (4):1247-1259.  
doi:10.1007/s11661-006-1076-9
17. Kim D, Badarinarayan H, Kim JH, Kim C, Okamoto K, Wagoner RH, Chung K (2010) Numerical simulation of friction stir butt welding process for AA5083-H18 sheets. *European Journal of Mechanics - A/Solids* 29 (2):204-215. doi:<http://dx.doi.org/10.1016/j.euromechsol.2009.10.006>

18. Rosenthal D (1941) Mathematical theory of heat distribution during welding and cutting. *Welding Journal* 20 (5):220-234
19. Schmidt HB, Hattel JH (2008) Thermal modelling of friction stir welding. *Scripta Materialia* 58 (5):332-337. doi:<http://dx.doi.org/10.1016/j.scriptamat.2007.10.008>
20. Darvazi AR, Iranmanesh M (2014) Thermal modeling of friction stir welding of stainless steel 304L. *The International Journal of Advanced Manufacturing Technology* 75 (9):1299-1307. doi:10.1007/s00170-014-6203-y
21. Bastier A, Maitournam MH, Dang Van K, Roger F (2006) Steady state thermomechanical modelling of friction stir welding. *Science and Technology of Welding and Joining* 11 (3):278-288. doi:10.1179/174329306X102093
22. Ávila RE (2006) A variational model for shear stress in friction stir welding based on the weld shape in transverse sections. *Modelling and Simulation in Materials Science and Engineering* 14 (4):689
23. Colegrove PA, Shercliff HR (2003) Experimental and numerical analysis of aluminium alloy 7075-T7351 friction stir welds. *Science and Technology of Welding & Joining* 8 (5):360-368. doi:10.1179/136217103225005534
24. Lienert TJ, Stellwag WL, Grimmer BB, Warke RW (2003) Friction Stir Welding Studies on Mild Steel. *Welding Journal* (January):1-9. doi:citeulike-article-id:12260782
25. Song M, Kovacevic R (2004) Heat transfer modelling for both workpiece and tool in the friction stir welding process: A coupled model. *Proceedings of the Institution of Mechanical Engineers, Part B: Journal of Engineering Manufacture* 218 (1):17-33. doi:10.1243/095440504772830174
26. Nandan R, Roy GG, Lienert TJ, DebRoy T (2006) Numerical modelling of 3D plastic flow and heat transfer during friction stir welding of stainless steel. *Science and Technology of Welding & Joining* 11 (5):526-537. doi:10.1179/174329306X107692
27. He Y, Boyce DE, Dawson PR (2007) Three-dimensional modeling of void growth in friction stir welding of stainless steel. *International Conference on Numerical Methods in Industrial Forming Processes* 908 (1):25-34. doi:10.1063/1.2740787
28. Abramowitz M, Stegun IA (1964) *Handbook of Mathematical Functions: With Formulas, Graphs, and Mathematical Tables*. Dover Publications,

### ***List of figures***

Fig.1. (a) Schematic diagram of the friction stir welding process and (b) the different heat generation regions.

Fig.2. Thermal conductivity and its average slope versus temperature [13-17].

Fig. 3. Fixed general coordinate (FC) and steady-state moving coordinate (MC) in FSW process.

Fig. 4. The velocity of one point on the tool shoulder.

Fig. 5. Definition of an element on the surface of the tool shoulder.

Fig. 6. Distance of one arbitrary point C from an element center.

Fig. 7. Definition of an element on the pin side.

Fig. 8. The suggested TMAZ profile for 304L stainless steel at advancing and retreating side.

Fig. 9. The shape of the TMAZ and definition of its boundary.

Fig. 10. Modeling of heat loss due to convection and radiation as a heat sink at top surface.

Fig. 11. The distribution of temperature for AA5083-H118 calculated via the present semi-analytical model induced by (a) the shoulder, (b) the pin, (c) the plastic dissipation in the TMAZ and (d) total temperature distribution for the welding condition of 800 rpm and 30 mm/min.

Fig.12. The algorithm of the numerical code for material updating written in Fortran language (in the present paper  $\delta T=1^{\circ}\text{C}$ ).

Fig. 13. Experimental installation (a) workpiece and thermocouple installation and (b) the Tool geometry.

Fig. 14. Comparison between experimental data [13] and calculated temperature histories on the top of the retreating side of the workpiece at various distance from the weld line for the translational speed of 102 mm/min and the rotational speed of 300 rpm.

Fig. 15. Comparison between the experimental data [13] and calculated temperature histories on the top of the retreating side of the workpiece at various distance from the weld line for the translational speed of 102 mm/min and the rotational speed of 500 rpm.

Fig. 16. Comparison between the experimental [24] and calculated temperature histories on the advancing side at a point 12.7 mm from the weld line for the translational speed of 25 mm/min and the rotational speed of 450 rpm.

Fig. 17. The temperature histories at various distance from the weld line for the rotational speed of 800 rpm and the translational speed of 100 mm/min.

Fig. 18. The temperature histories at various distance from the weld line for the rotational speed of 1100 rpm and the translational speed of 100 mm/min.

Fig. 19. The temperature histories at various distance from the weld line for the rotational speed of 1400 rpm and the translational speed of 100 mm/min.

Fig. 20. Comparison between the experimental [25] and calculated temperature histories at points 2 mm below the top surface at distance of ( a ) 8 mm and ( b ) 16 mm from the centerline for the rotational speed of 1400 rpm and the translational speed of 100 mm/min.

Fig. 21. Comparison between the experimental [25] and calculated temperature histories at different locations for welding conditions of (a) 220 rpm and 220 mm/min, and ( b ) 457 rpm and 457 mm/min.

Fig.22. Schematic of any element of shoulder region as a heat source.

Fig.23. Modeling of heat source: (a) the Ferro and Bonollo model [4] and (b) the present model.

Fig. 24. The Computed temperature profiles on the top surface of workpiece for the rotational speed of 300 rpm and the translational speed of 102 mm/min: (a) Nandan et al. [26], (b) Darvazi et al. [20], (c) He et al. [27] and (d) The present work.

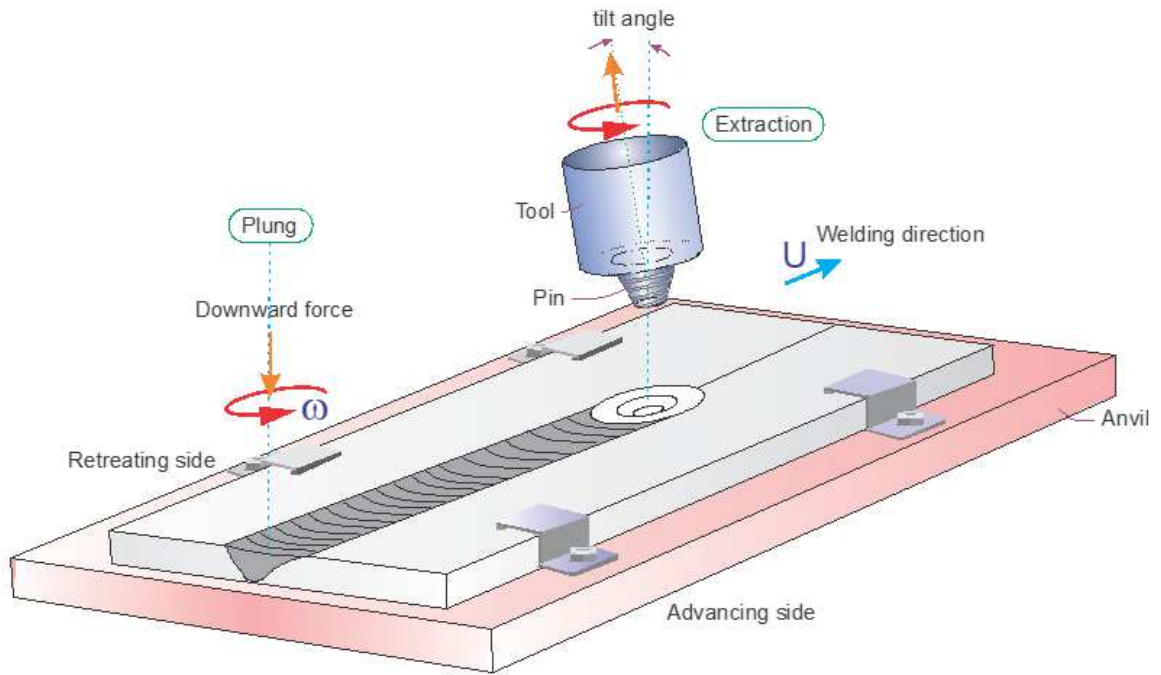
Fig.25. The cross-sectional temperature distribution of the FSW in the transverse direction computed by: a) Darvazi et al. [20] and b) the present method.

***List of Tables***

Table I. The data used in the simulation of the FSW of aluminum alloys and steels.

# Figures

(a)



(b)

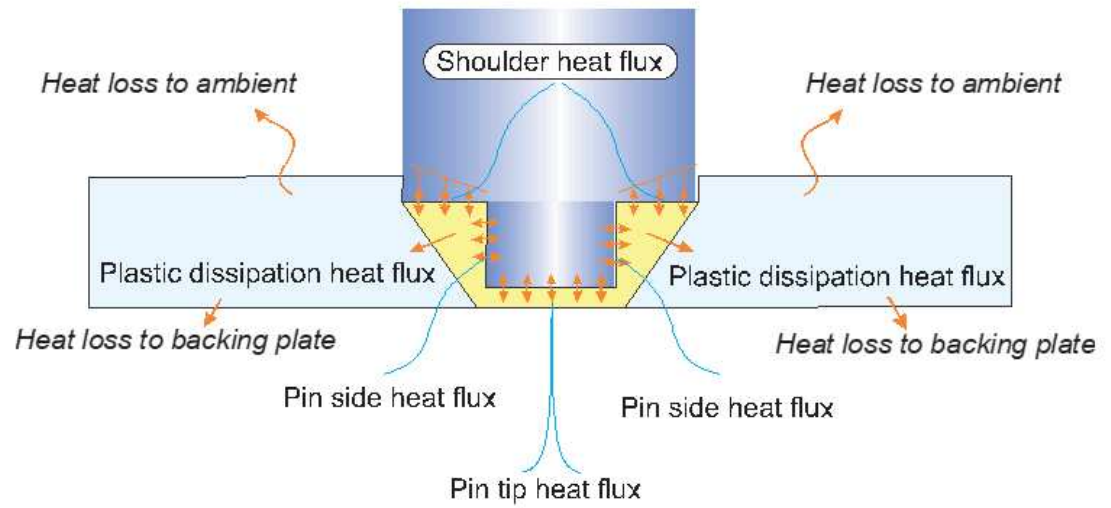


Figure 1

(a) Schematic diagram of the friction stir welding process and (b) the different heat generation regions

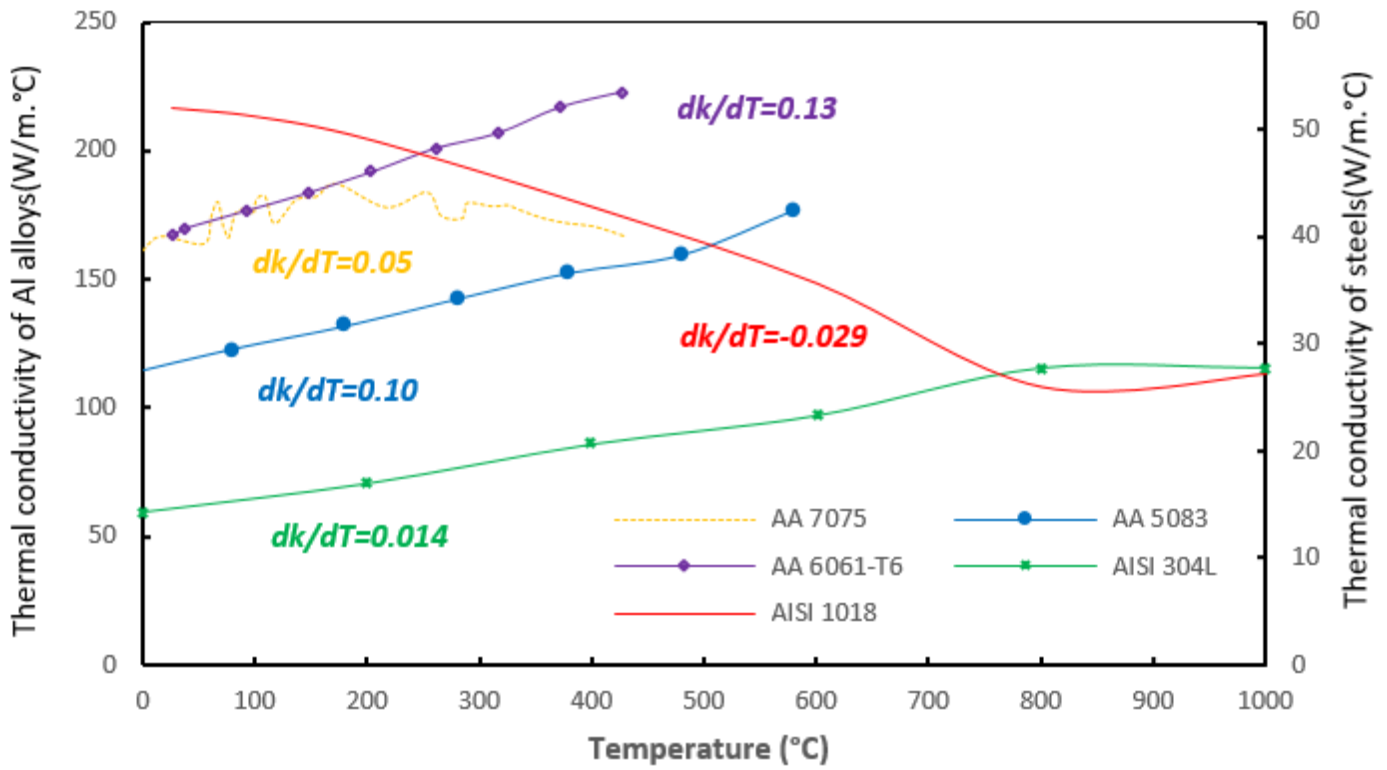


Figure 2

Thermal conductivity and its average slop versus temperature [13-17].

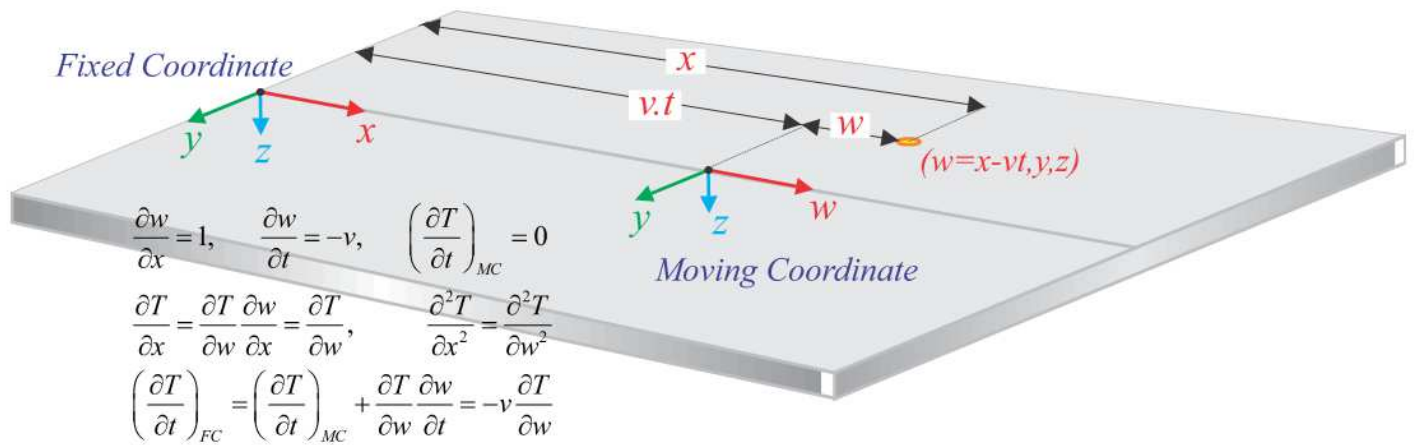


Figure 3

Fixed general coordinate (FC) and steady-state moving coordinate (MC) in the FSW process.

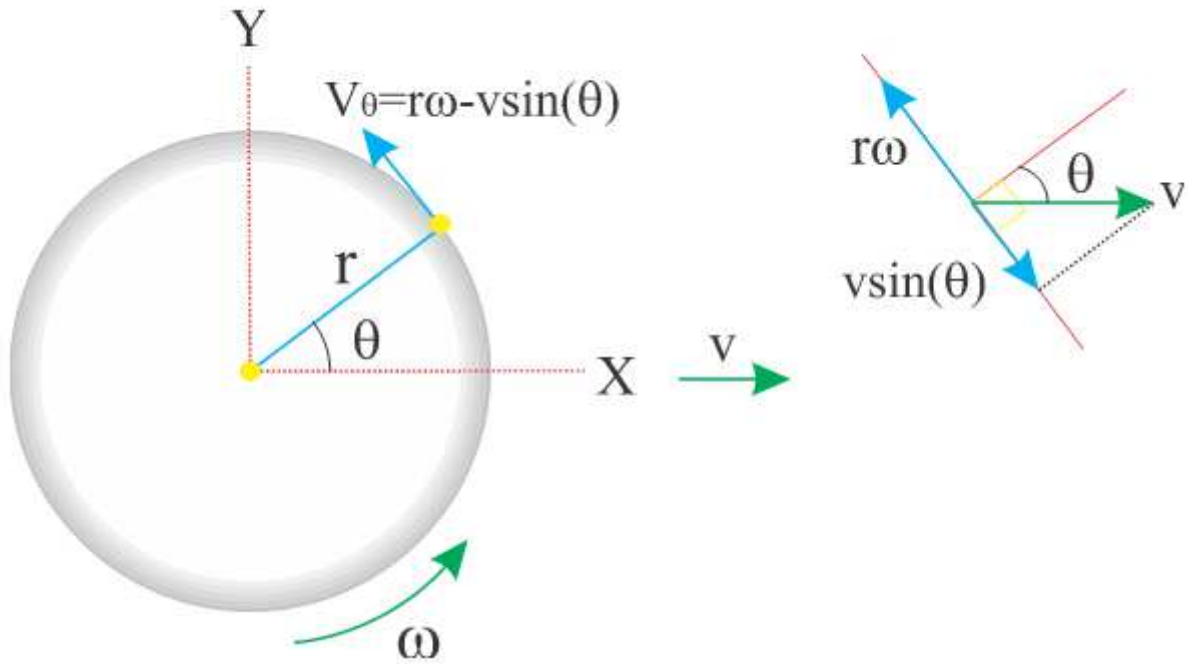
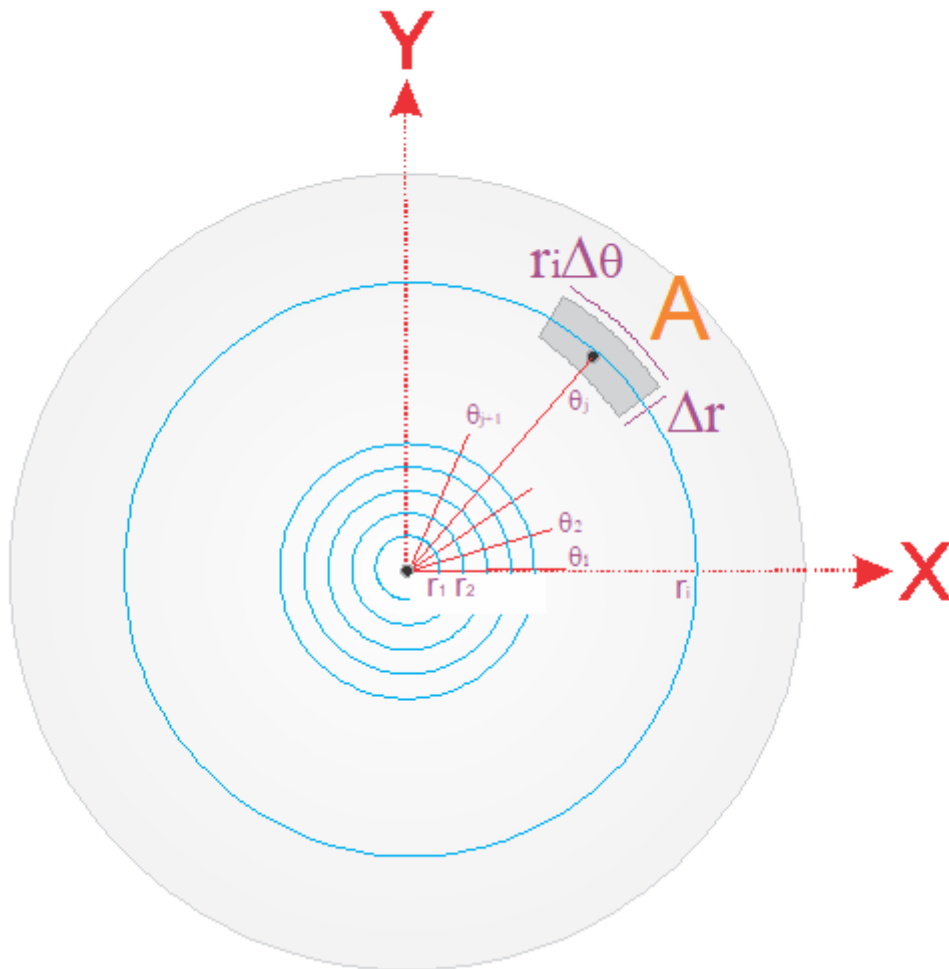


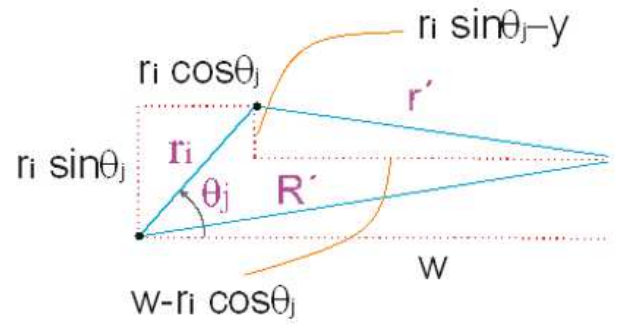
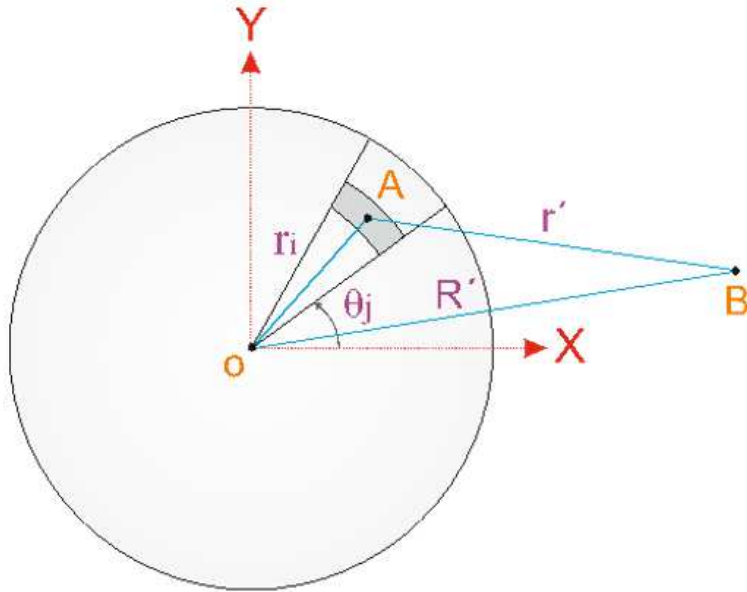
Figure 4

The velocity of one point on the tool shoulder.



**Figure 5**

Definition of an element on the surface of the tool shoulder.



$$r' = \sqrt{(w - r_i \cos \theta_j)^2 + (y - r_i \sin \theta_j)^2}$$

$$R = \sqrt{(w - r_i \cos \theta_j)^2 + (y - r_i \sin \theta_j)^2 + z^2}$$

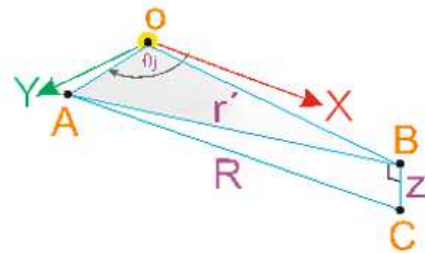


**Figure 6**

The distance of one arbitrary point C from an element center.

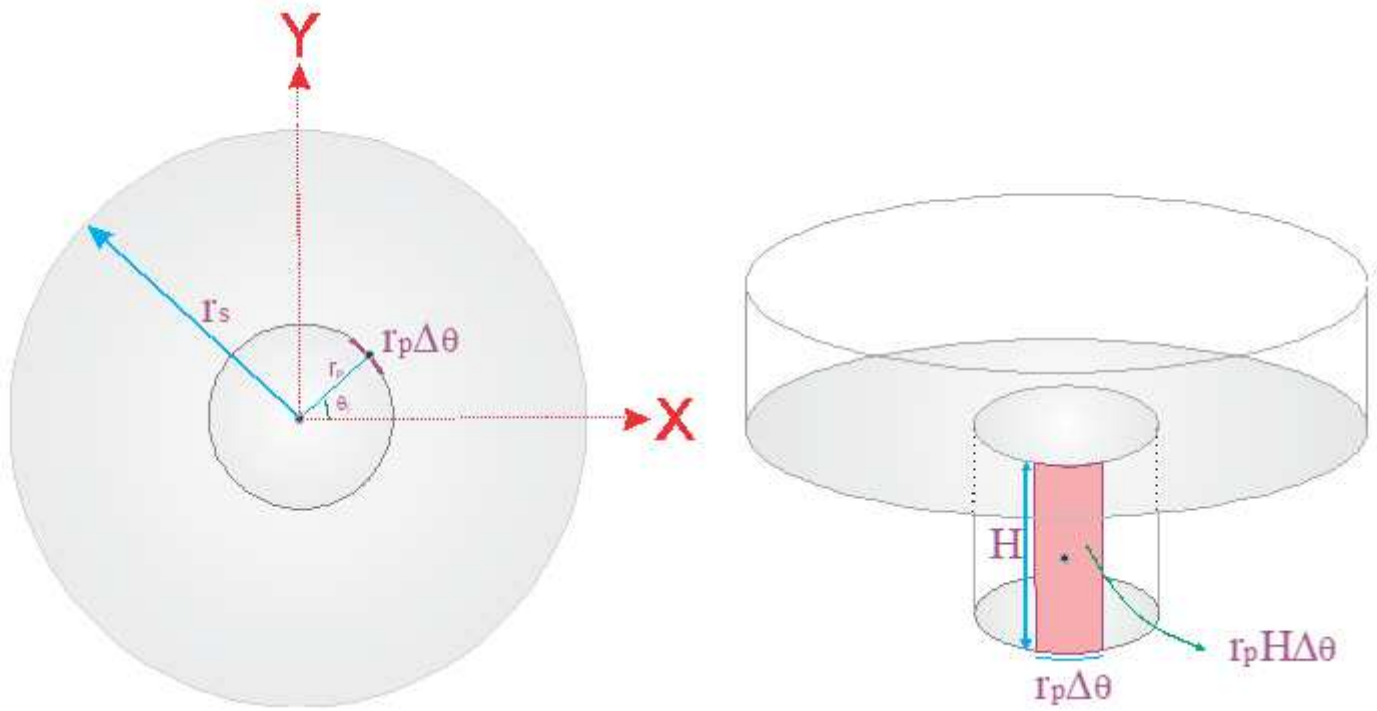


**Figure 7**

Definition of an element on the pin side.

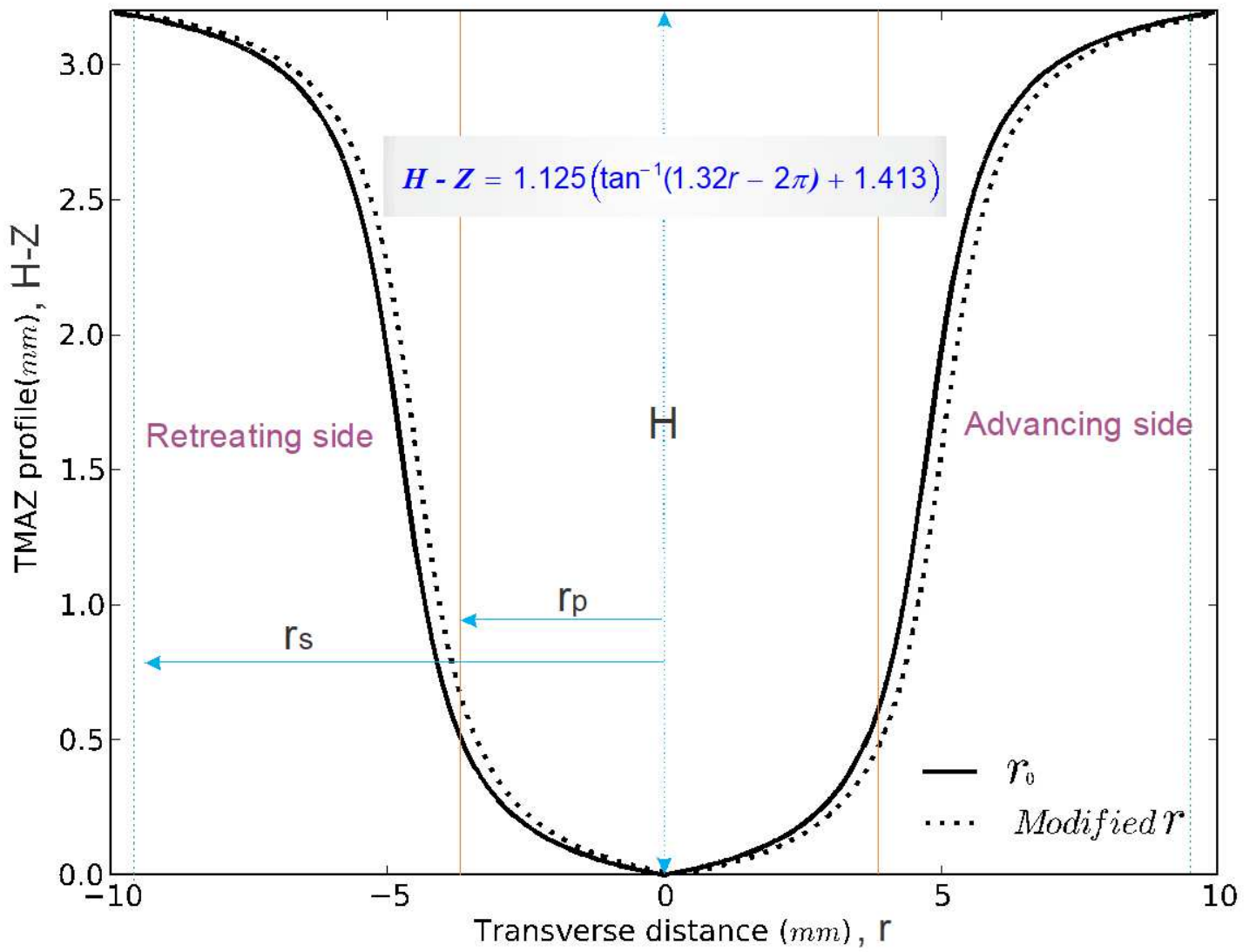


Figure 8

The suggested TMAZ profile for 304L stainless steel at advancing and retreating side.

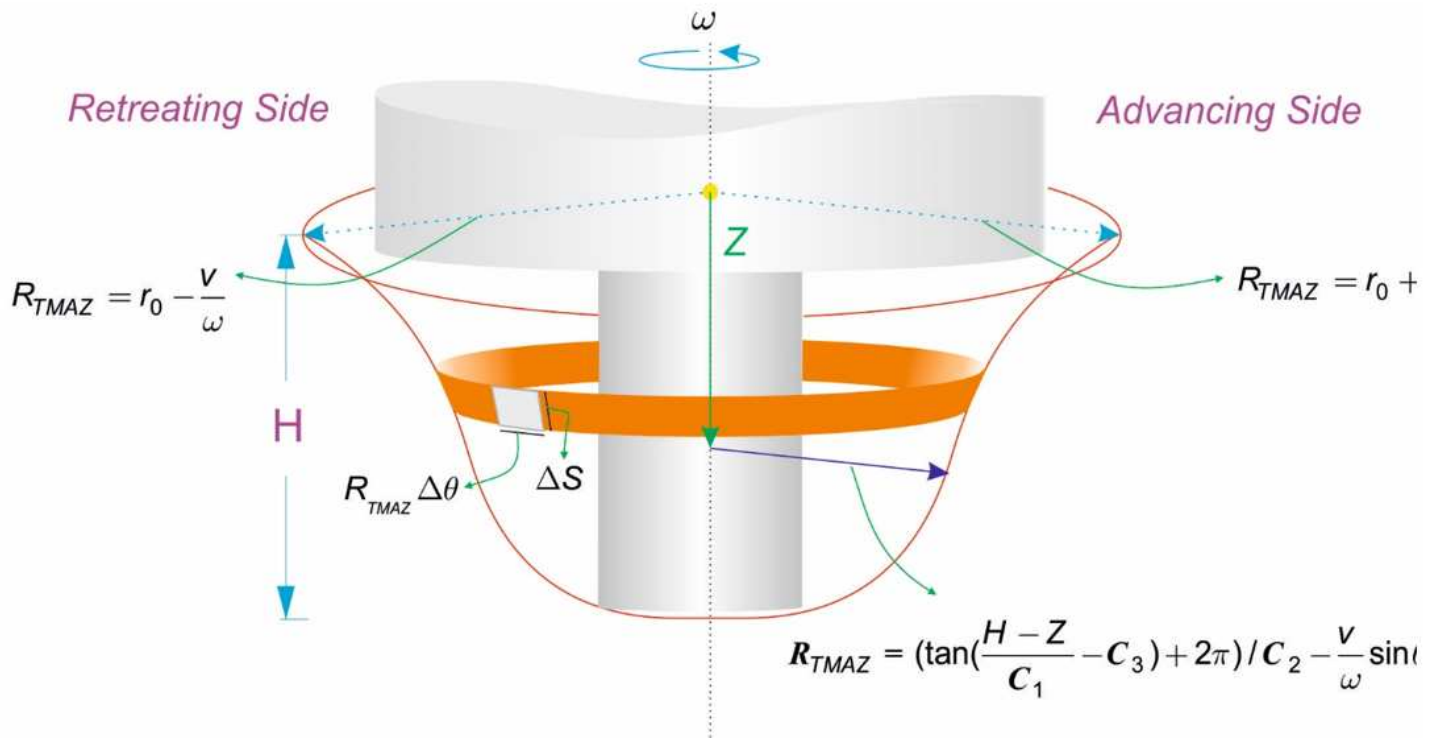


Figure 9

The shape of the TMAZ and definition of its boundary.

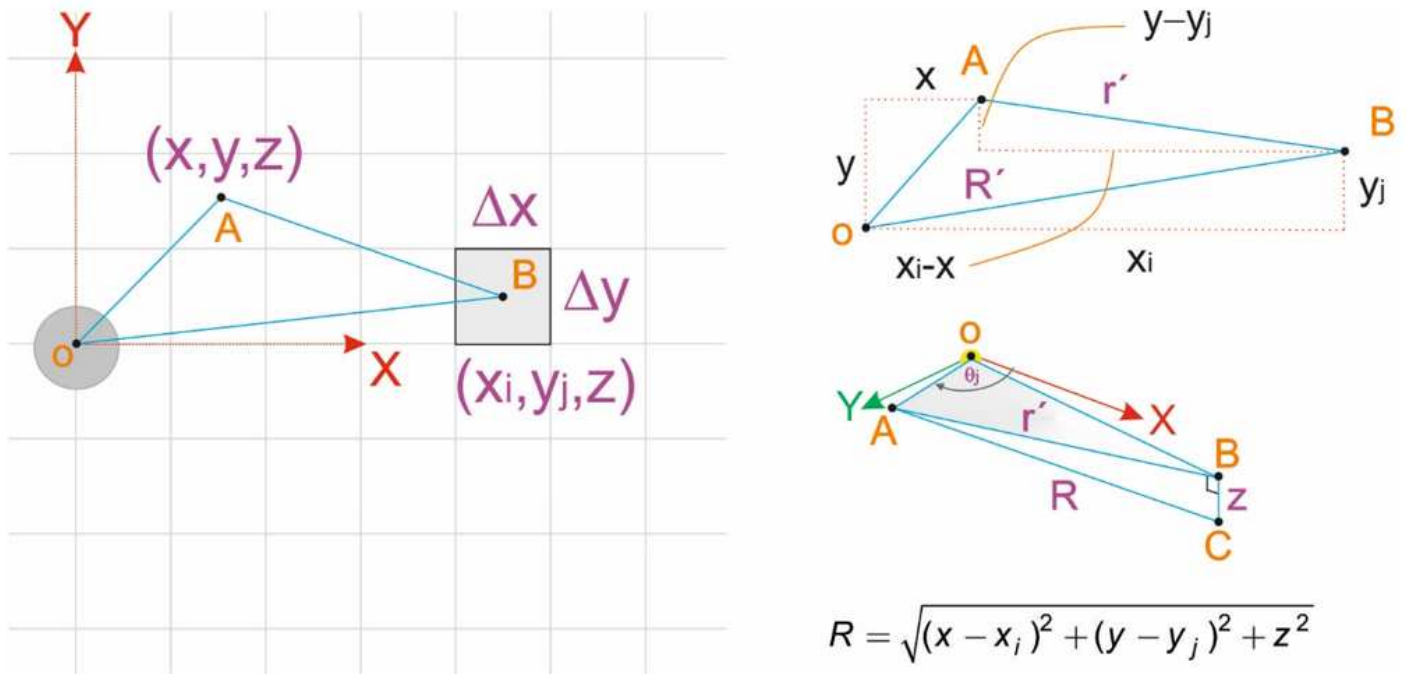
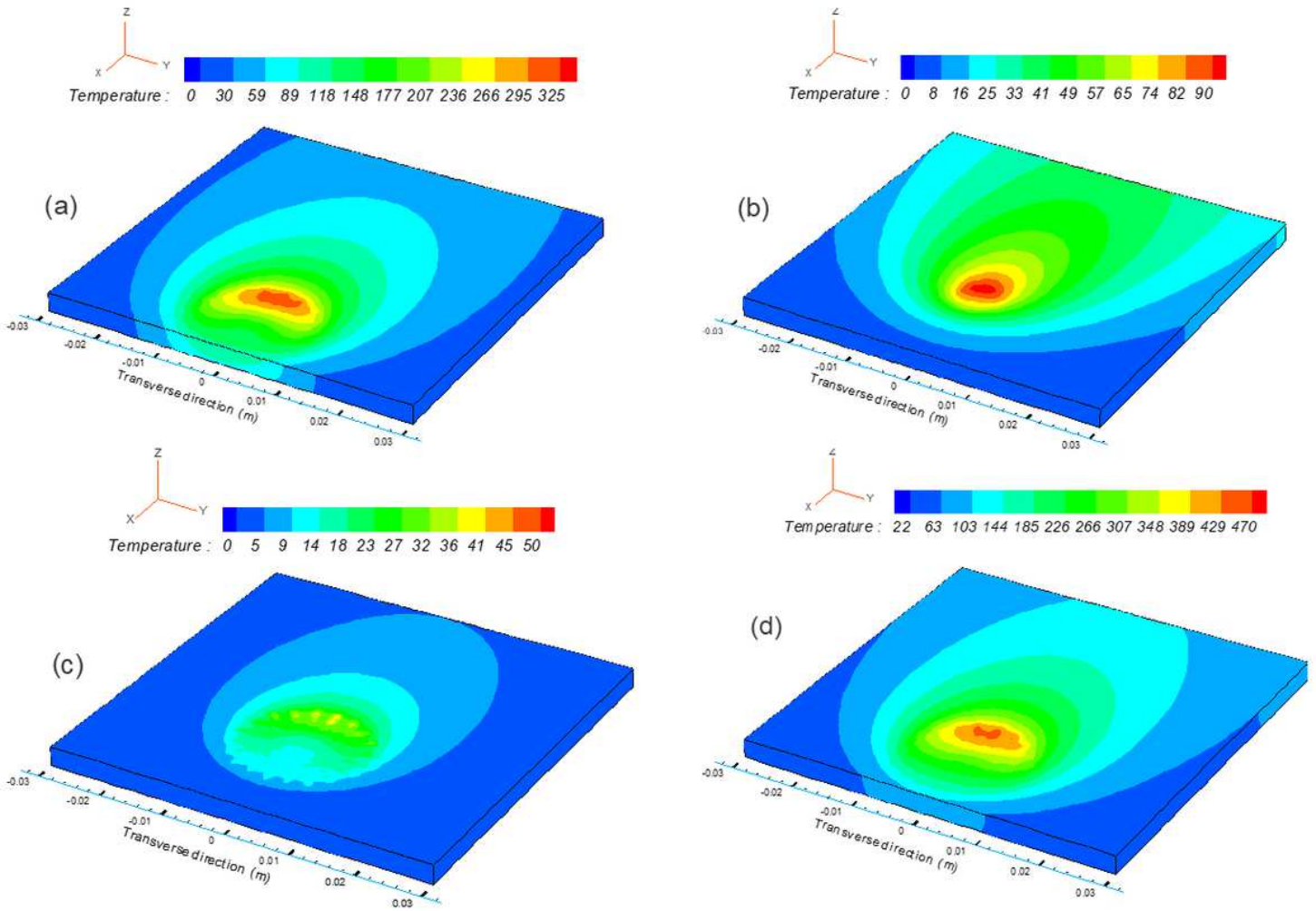


Figure 10

Modeling of heat loss due to convection and radiation as a heat sink at the top surface



**Figure 11**

The distribution of temperature for AA5083-H118 calculated via the present semi-analytical model induced by (a) the shoulder, (b) the pin, (c) the plastic dissipation in TMAZ and (d) total temperature for the welding condition of 800 rpm and 30 mm/min.

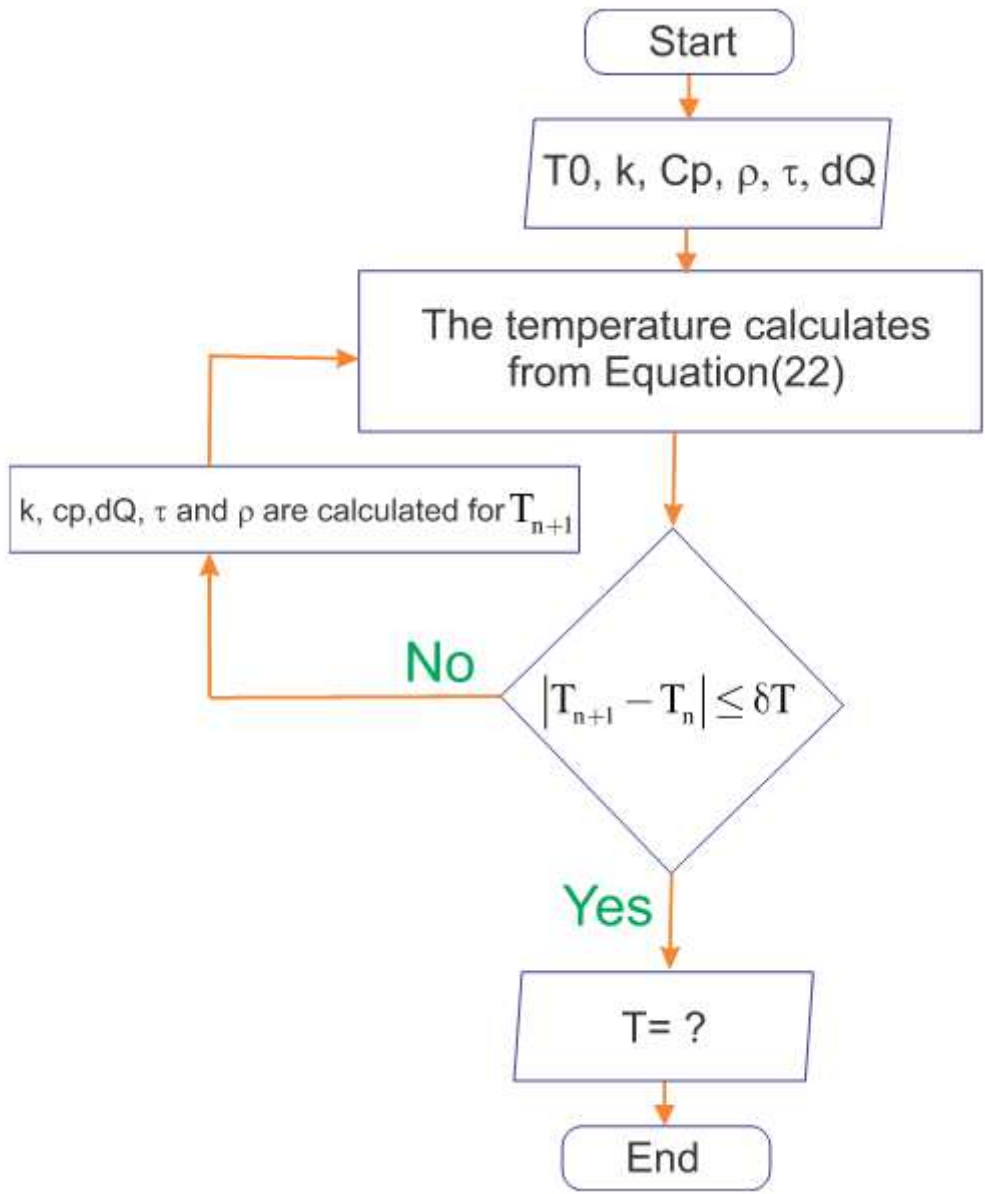


**Figure 12**

The algorithm of the numerical code for material updating written in Fortran language (in the present paper  $\delta T=1^{\circ}\text{C}$ ).

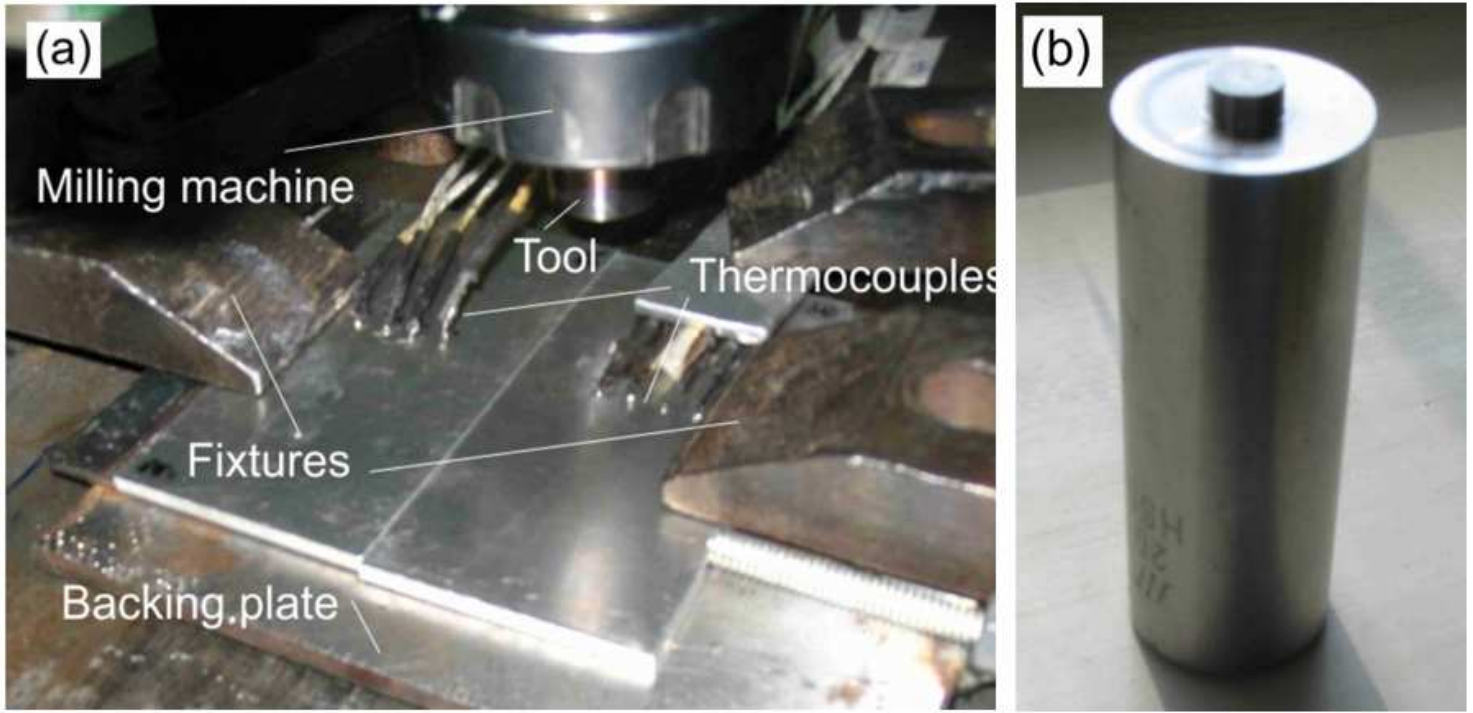


Figure 13

Experimental installation (a) workpiece and thermocouple installation and (b) the Tool geometry.

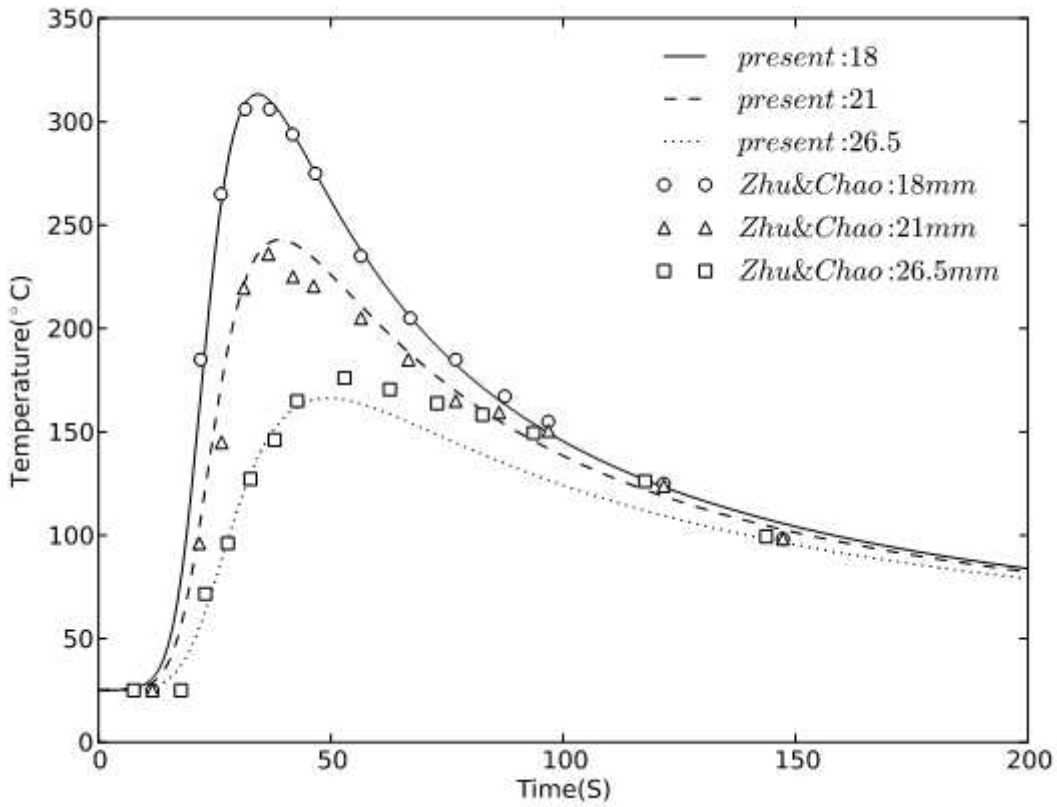
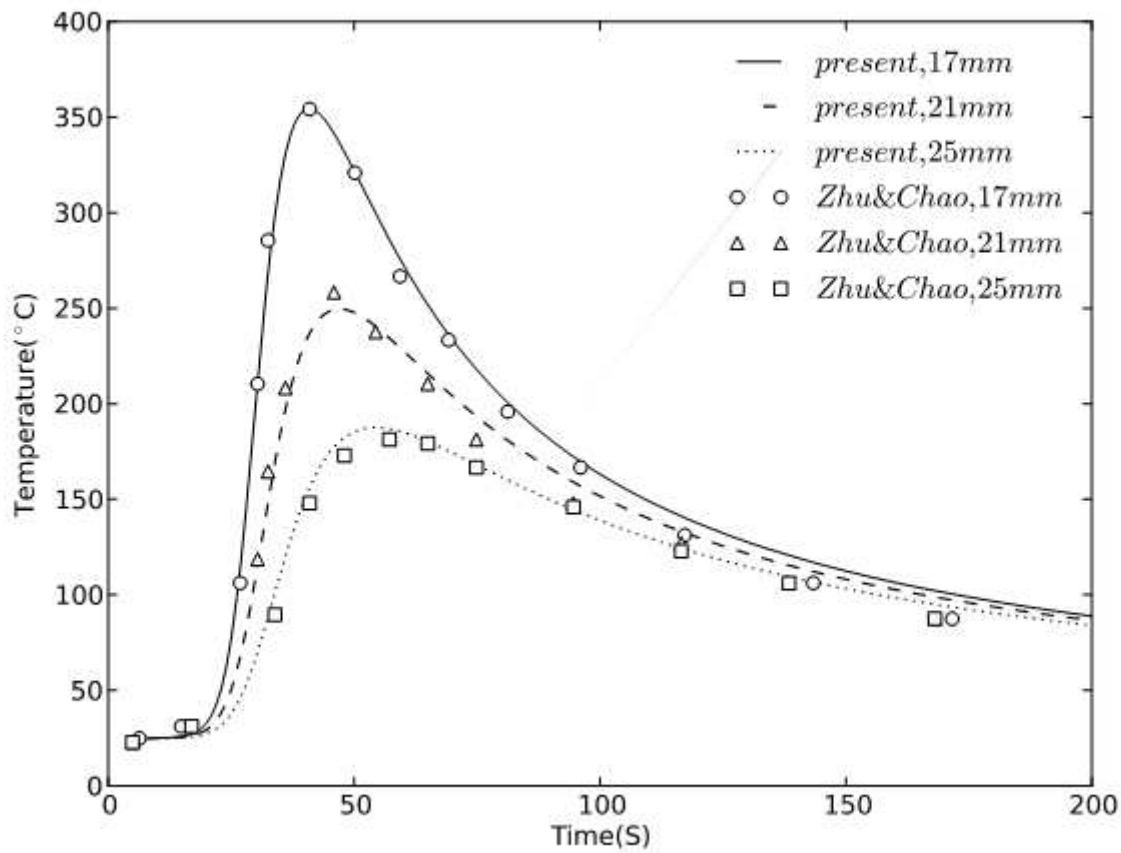


Figure 14

Comparison between the experimental data [13] and calculated temperature histories on the top of the retreating side of the workpiece at various distance from the weld line for the translational speed of 102 mm/min and the rotational speed of 300 rpm.



**Figure 15**

Comparison between the experimental data [13] and calculated temperature histories on the top of the retreating side of the workpiece at various distance from the weld line for the translational speed of 102 mm/min and the rotational speed of 500 rpm.

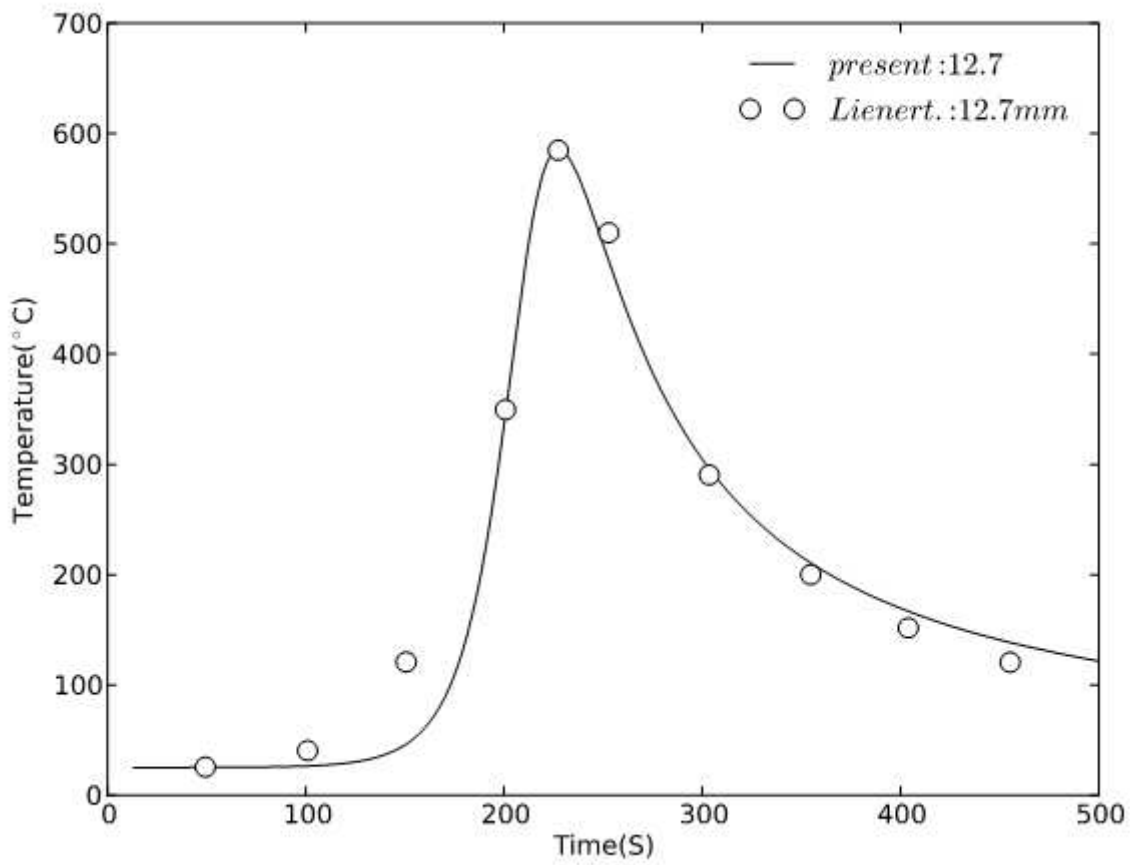


**Figure 16**

Comparison between the experimental [24] and calculated temperature histories on the advancing side at a point 12.7 mm from the weld line for the translational speed of 25 mm/min and the rotational speed of 450 rpm.

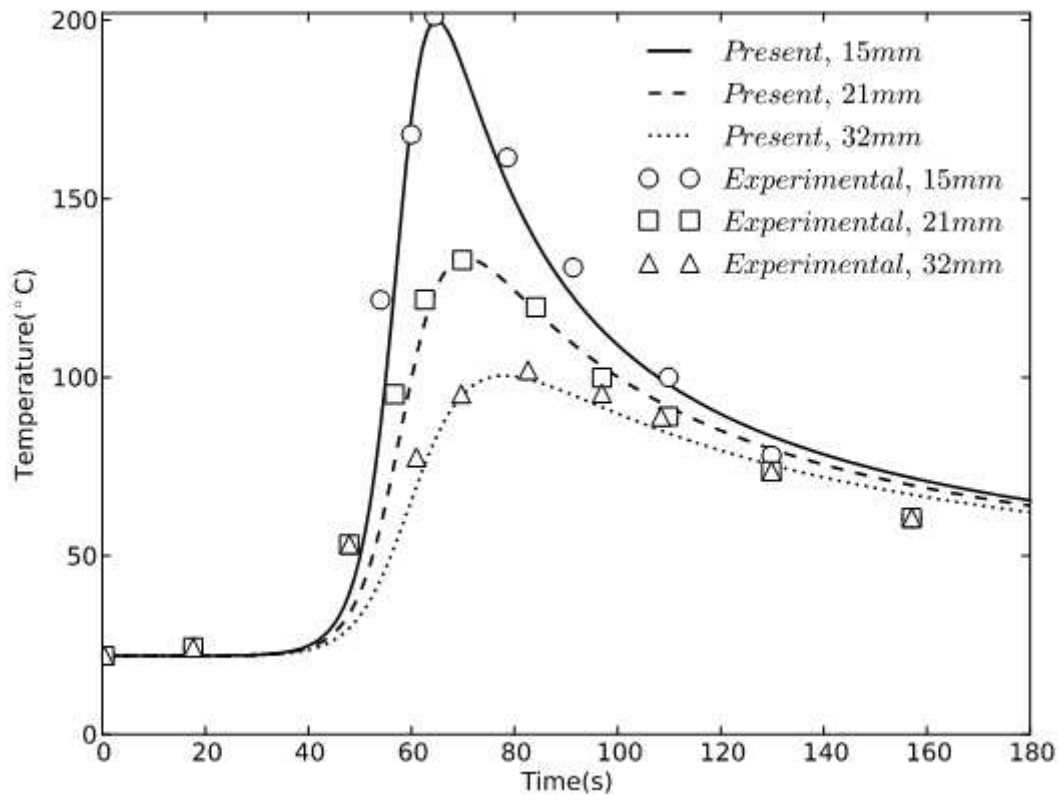


**Figure 17**

The temperature histories at various distance from the weld line for the rotational speed of 800 rpm and the translational speed of 100 mm/min.

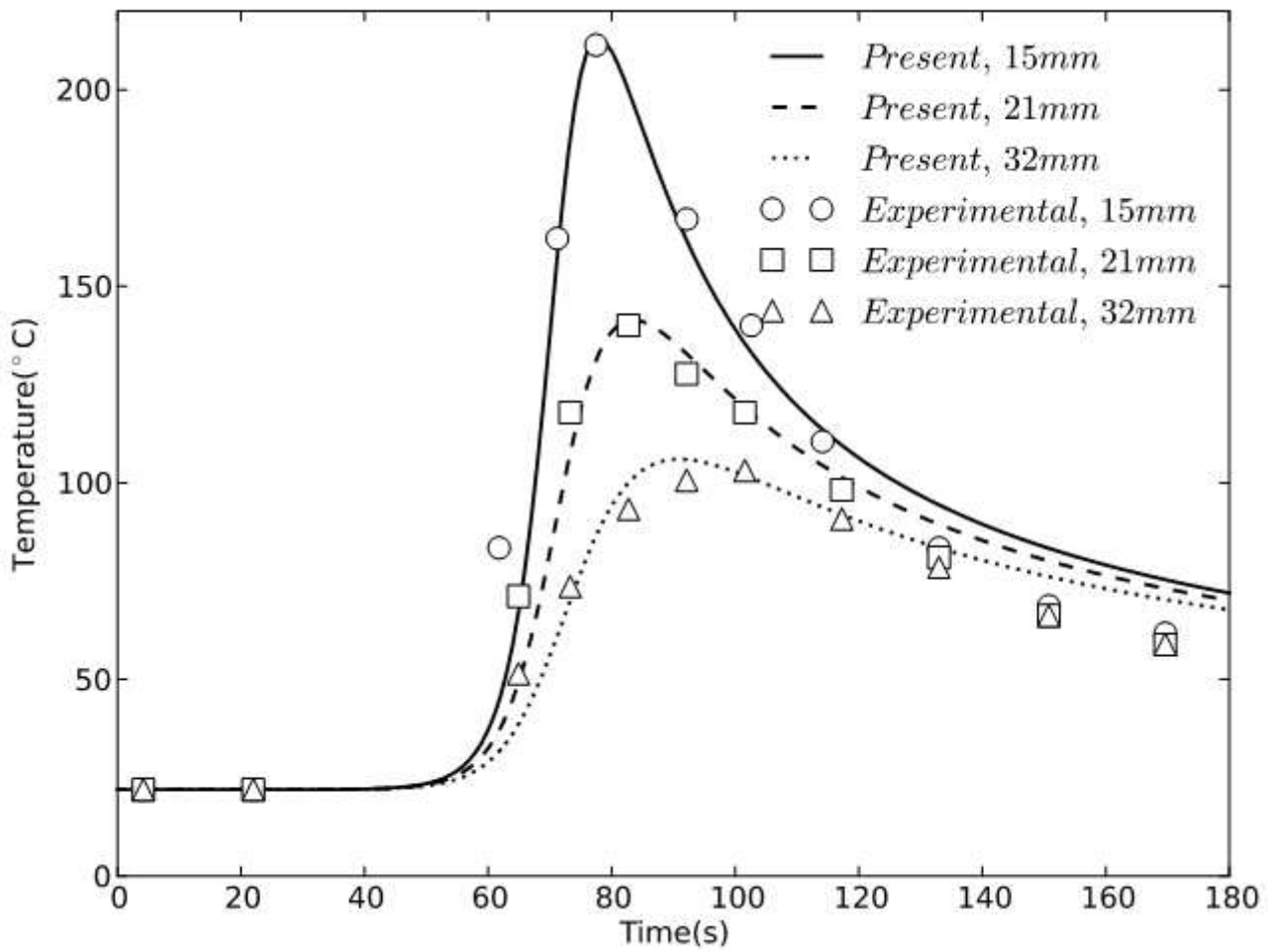


**Figure 18**

The temperature histories at various distance from the weld line for the rotational speed of 1100 rpm and the translational speed of 100 mm/min.

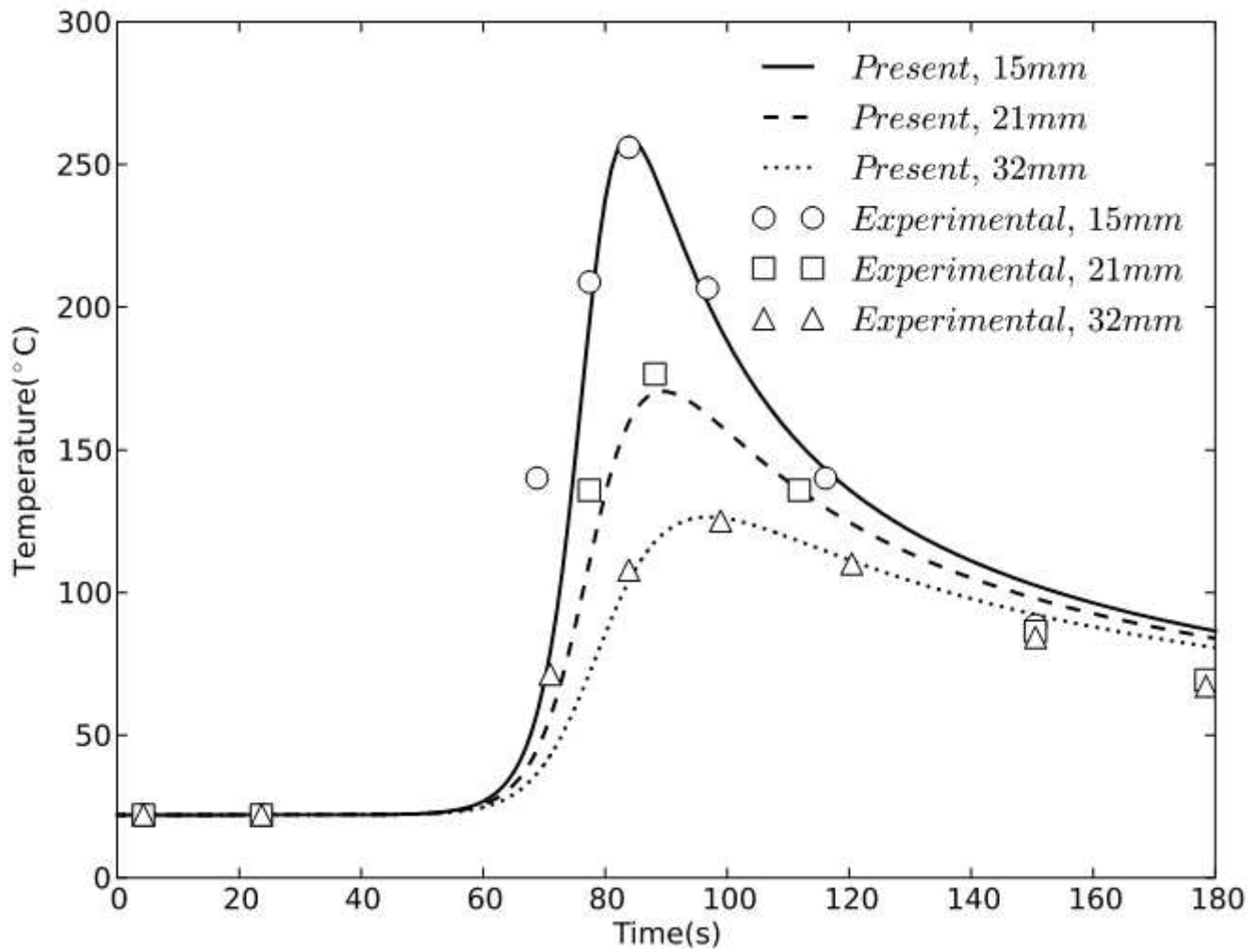
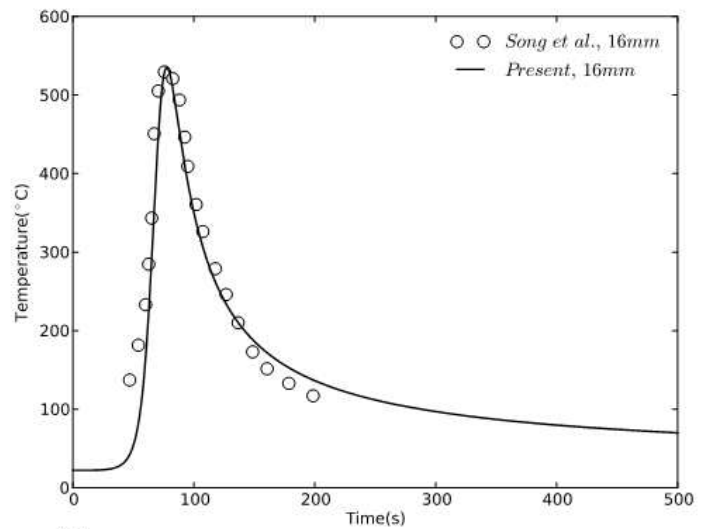
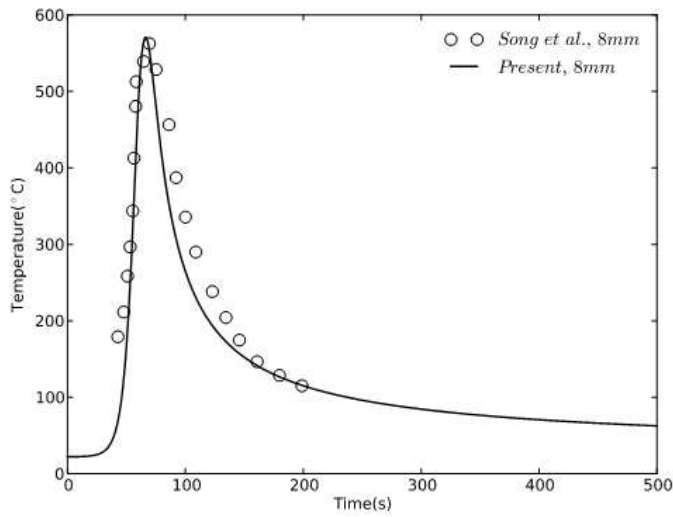


**Figure 19**

The temperature histories at various distance from the weld line for the rotational speed of 1400 rpm and the translational speed of 100 mm/min.



(a)

(b)

**Figure 20**

Comparison between the experimental [25] and calculated temperature histories at points 2 mm below the top surface at a distance of (a) 8 mm and (b) 16 mm from the centerline for the rotational speed of 1400 rpm and the translational speed of 100 mm/min.

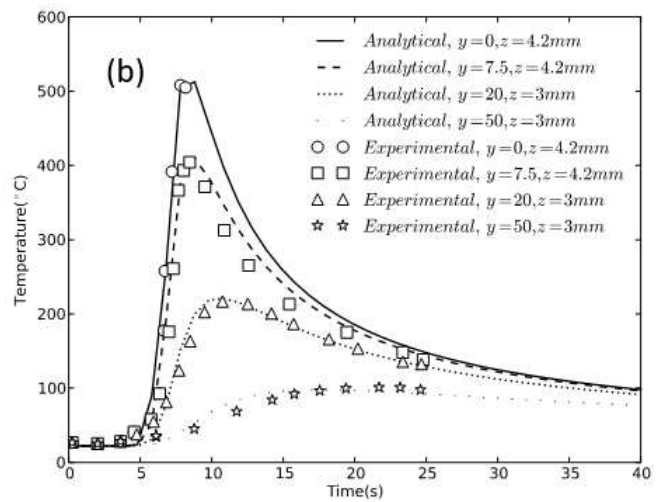
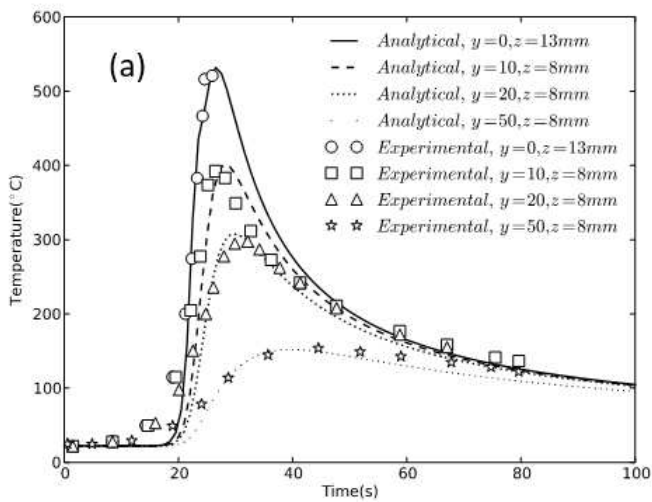


**Figure 21**

Comparison between the experimental [23] and calculated temperature histories at different locations for welding conditions of (a) 220 rpm and 220 mm/min, and (b) 457 rpm and 457 mm/min.

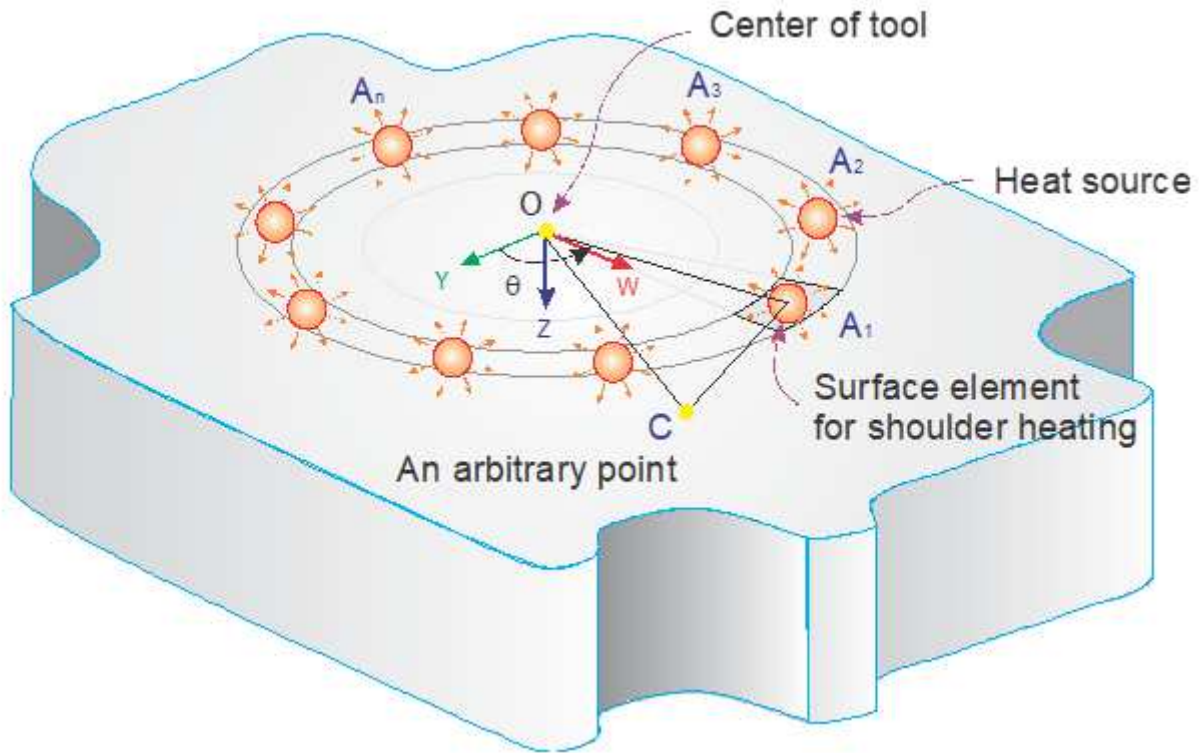


**Figure 22**

Schematic of any element of the shoulder region as a heat source.

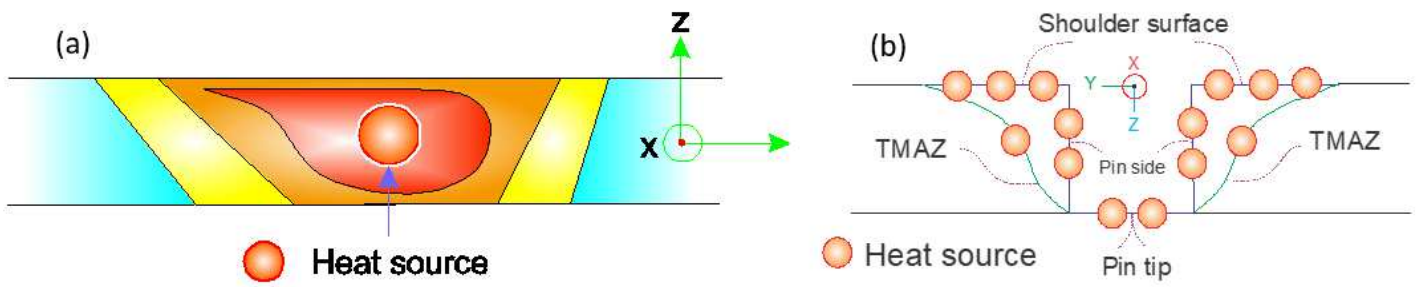


**Figure 23**

Modeling of heat source: (a) the Ferro and Bonollo model [4] and (b) the present model.

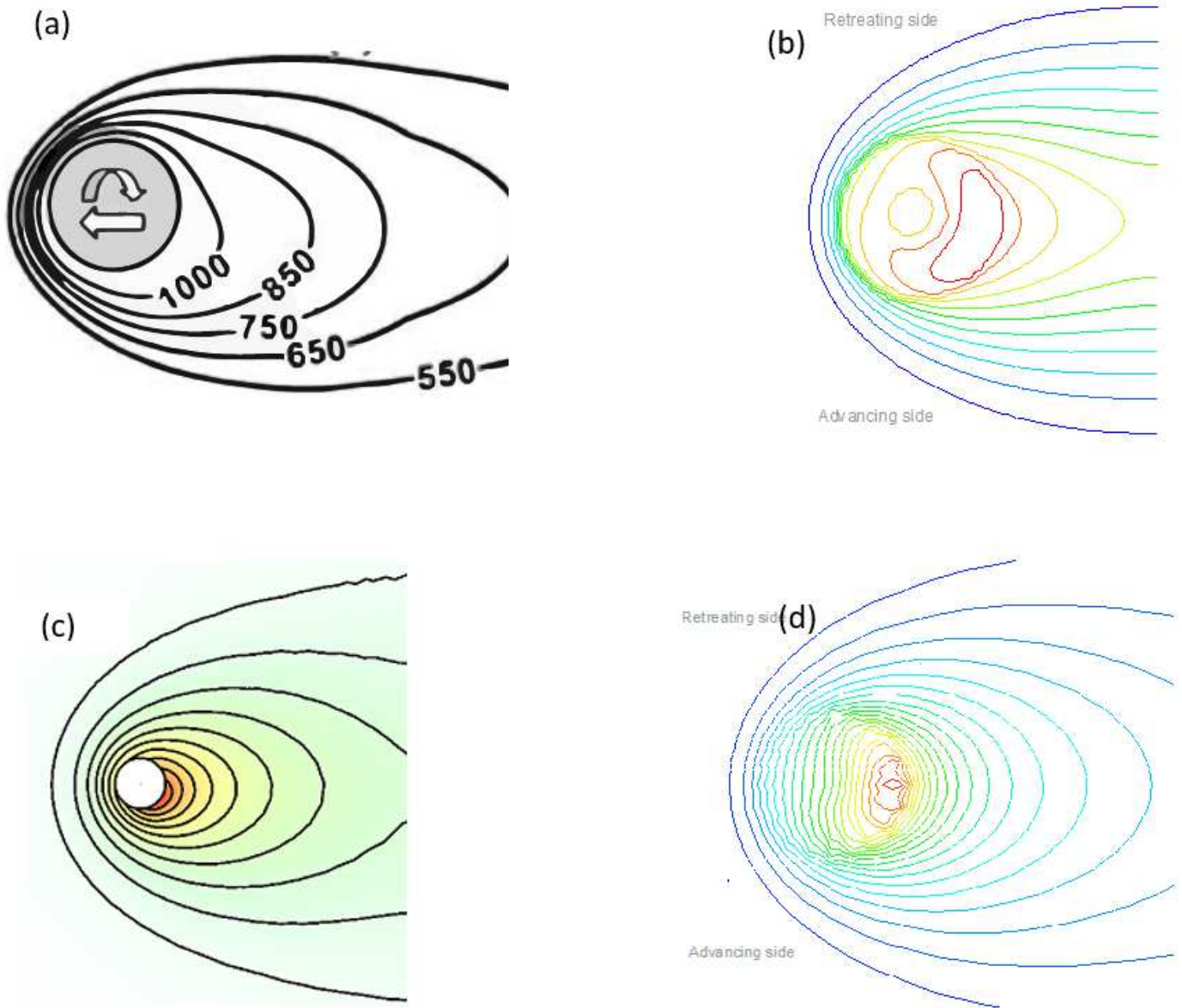


**Figure 24**

The Computed temperature profiles on the top surface of workpiece for the rotational speed of 300 rpm and the translational speed of 102 mm/min: (a) Nandan et al. [26], (b) Darvazi et al. [20], (c) He et al. [27] and (d) The present work.

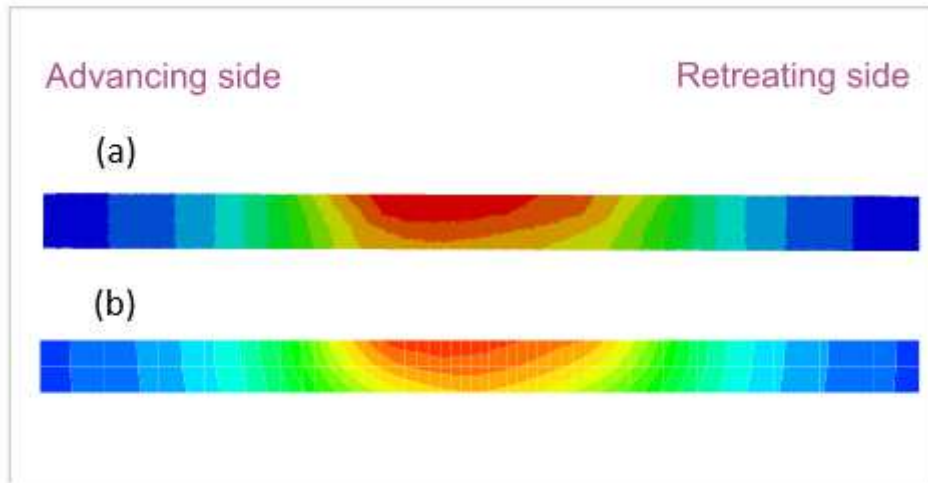


**Figure 25**

The cross-sectional temperature distribution of the FSW in the transverse direction computed by: a) Darvazi et al. [20] and b) the present method.

## Supplementary Files

This is a list of supplementary files associated with this preprint. Click to download.

- [GraphicalAbstract.docx](#)